ANALYSIS OF IMPEDANCE RESPONSE IN LITHIUM-ION BATTERY ELECTRODES

A Thesis

by

SEONGKOO CHO

Submitted to the Office of Graduate and Professional Studies of
Texas A&M University
in partial fulfillment of the requirements for the degree of

MASTER OF SCIENCE

Chair of Committee,	Partha P. Mukherjee
Committee Members,	Xinghang Zhang
	Philip Park
Head of Department,	Andreas A. Polycarpou

December 2013

Major Subject: Mechanical Engineering

ABSTRACT

A major amount of degradation in battery life is in the form of chemical degradation due to the formation of Solid Electrolyte Interface (SEI) which is a passive film resulting from chemical reaction. Mechanical degradation in the form of fracture formation due to diffusion induced stress can aggravate the aging of the electrode. These mechanisms of deterioration are primary contributors on limiting the durability of Lithium-ion battery (LIB). In addition, an composition of insertion materials such as active material, additive, and binder as well as active particle's morphological heterogeneity can influence solid-state transport, electronic conductivity and hence, battery performance.

In this study, virtual 3-D microstructures of LIB electrodes with intercalation particles are designed to describe the influence of microstructure on effective electrical conductivity and the electrochemical impedance. The technique of digital stochastic modeling has been employed for the generation of electrode microstructures consisting of active material, binder, conductive additive and electrolyte. Physicochemical properties for each of the constituent phases have been duly accounted for. Mathematical models have been developed to characterize the electrochemical impedance of LIB electrode. In this work, we demonstrate the coupling of electrode microstructures to the solid state diffusion impedance response in LIB electrodes. This model considers not only the effect of heterogeneity in active particle size on the diffusion impedance response, but also the effect of electrical conductivity, interfacial surface area of the

active materials, and volume fraction of the active materials in the porous electrode on the impedance response. In addition, the impact of the morphology of the active materials on the diffusion impedance response through utilization of the characteristic diffusion length of active particles and a Sauter mean particle size has been demonstrated.

In order to show the effect of chemical degradation on the impedance response with focus on aging, the Li-ion diffusion inside an active particle is considered along with SEI. Finally, mechanical degradation induced increase in impedance is analyzed by coupling diffusion induced fracture with impedance. These approaches are envisioned to offer a virtual impedance response probing framework to elucidate the influence of electrode microstructural variability and underlying electrochemical and transport interactions.

DEDICATION

To my family

ACKNOWLEDGEMENTS

I would like to thank my committee chair, Dr. Mukherjee, for his instruction and encouragement all over the course of this work. I also thank my committee members, Dr. Zhang and Dr. Park, for their valuable advice and for their careful review of this thesis.

Thanks also go to all ETSL teammates for making my time at Texas A&M University a great experience.

Finally, I want to extend my gratitude to my friends and colleagues, who have come into my life during the last two years.

NOMENCLATURE

F	Faraday's Constant
R	Universal Gas Constant
T	Temperature
$\dot{I}$	Source Term
V	Potential
U	Open Circuit Potential
CV	Coefficient of Variation
i_0	Exchange Current Density
i_{inf}	Interfacial Current Density
i_{dbl}	Non-faradaic Current Density or Double Layer Current Density
i_{far}	Faradaic Current Density
c_i	Concentration of Intercalation Ions in a Single Active Particle
$\tilde{c}_i\left(R_i\right)$	Surface Concentration of a Single Particle
C_{dbl}	Capacity of the Double Layer
r	Distance from the Symmetric Center of the Active Material Particles
t	Time Variable
D_a	Diffusion Coefficient of the Active Material
Z_{dbl}	Impedance for a Non-Faradaic Reaction

Z_i	Local Bounded Diffusion Impedance of a Single Active Particle
R_{ctr}	Charge Transfer Impedance
$Z_{total,i}$	Impedance of an Effective Single Particle
Z_{EM}	Overall Impedance of the Porous Electrode Microstructure
d_{smd}	Sauter Mean Diameter
V_P	Volume of the Particle
A_P	Effective Surface Area of the Particle
$A_i(r_i)$	Effective Surface Area at a Specific r_i
$N_i(r_i)$	Number of Active Material Particles per Unit Electrode Volume with Distance r_i from the Symmetric Center of the Active Particles
N_{total}	Number of Total Active Particles per Unit Electrode Volume
$P_i(r_i)$	Probability Density Function
$r_{smd,i}$	Sauter Mean Radius
NR_i	Particle Number Ratio

Greek

α_a	Anodic Transfer Coefficient
α_c	Cathodic Transfer Coefficient
α, β, γ	Aspect Ratio

Φ_D	Total Domain under Consideration
ϕ_1	Potential at an Active Particle Interface between Active Particle and Film
$\phi_{1\text{flm}}$	Potential at a Film Interface between Active Particle and Film
μ_{CV}	Arithmetic Mean of Effective Conductivity
σ_{CV}	Standard Deviation of Effective Conductivity
σ_L	Local Electrical Conductivity
σ	Solid-Phase Electrical Conductivity
κ	Electrical Conductivity of Electrolyte

Superscripts

~	Frequency Domain

Subscripts

i	Particle Morphology
sp	Sphere
cy	Cylinder
pl	Platelet

TABLE OF CONTENTS

Page

ABSTRACT ii

DEDICATION iv

ACKNOWLEDGEMENTS v

NOMENCLATURE vi

TABLE OF CONTENTS ix

LIST OF FIGURES xi

LIST OF TABLES xv

CHAPTER I INTRODUCTION AND LITERATURE REVIEW 1

Electrochemical Impedance Spectroscopy 4
Chemical and Mechanical Degradation 5

CHAPTER II MODEL DESCRIPTION 7

Mathematical Model for the Impedance Response of a Single Particle 7
Non-faradaic Impedance 8
Faradaic Impedance 9
Impedance of an Effective Single Particle 13
Impedance of 3-D Electrode Microstructure 15
Particle Size Distribution and Sauter Mean Diameter 15
Overall Impedance of 3-D Electrode 18
Stochastic Microstructure Generation and Electrical Conductivity Evaluation 19
Stochastic Generation of Electrode Microstructure 19
Effective Electrical Conductivity 20

CHAPTER III ANALYSIS OF THE EFFECT OF MICROSTRUCTURES ON THE IMPEDANCE RESPONSE 24

Influence of Porous Electrode Microstructure on the Impedance Response 24
Effect of Morphology of Active Materials on Diffusion Impedance Response of the 3D Electrode Microstructure 34

CHAPTER IV EFFECT OF THE CHEMICAL DEGRADATION ON IMPEDANCE RESPONSE 41

Mathematical Model for a Single Active Particle with SEI 41
Impedance Response for a Single Intercalation Particle Consisting of an SEI 45

CHAPTER V EFFECT OF THE MECHANICAL DEGRADATION ON IMPEDANCE RESPONSE 51

CHAPTER VI SUMMARY AND OUTLOOK 59

Future Work 61

REFERENCES 62

LIST OF FIGURES

Page

Figure 1. The schematic of the active particles - interfacial impedance with solid-phase diffusion but no insulating film for a single particle; (a) Various morphologies of single active particles, (b) equivalent circuit design 8

Figure 2. Local bounded diffusion impedance for various particle morphologies. 13

Figure 3. Nyquist plot of impedance of a single particle for interfacial impedance with solid-phase diffusion limitations but no insulating film 14

Figure 4. The diameter design of a sphere that has the same ratio of particle volume to effective surface area as a particle of interest; (a) The relation between an amorphous particle and a sauter mean particle. Ap and Vp are the effective surface area and the particle volume, respectively. (b) The sauter mean diameters of a cylindrical particle and a platelet particle. $\alpha, \beta,$ and γ are aspect constants 16

Figure 5. The balance diagram on the fraction of total current flowing 18

Figure 6. Full 3D microstructure electrode model with (a) Spherical active particles (b) Cylindrical active particles (c) Platelet active particles 21

Figure 7. Schematic of conductive additive 22

Figure 8. The coefficient of variation for evaluated electrode microstructures. 23

Figure 9. Dependence of the local bounded impedance response on the electrical conductivity of 3D porous electrodes. The mean radius of spherical active particles is 2.9823um and the volume fraction of spherical active particles is 39.19%. The specific surface area is 3883.02cm-1. The volume fraction of electrolyte is 35 %. (a) Active particle size distribution and 3D microstructures with various combinations of electrolyte, binder, and additive. The ratio of additive to binder and the conductivities of electrolyte(S/cm) are (i) 0.101:1, 0.01, (ii) 0.2:1, 0.01, (iii) 0.324:1, 0.01, (iv) 0.324:1, 0.0001, (v) 0.324:1, 0.00005, and (vi) 0.324:1, 0.00001, respectively. (b) Nyquist plot of impedance response in 3D electrodes. (c) Magnitude image. (d) Phase angle plot. 26

Figure 10. Effect of the specific surface area of active materials on the impedance response of the 3-D microstructure electrode. The mean radius of spherical active particles is approximately 3 μm (i. 3.0031 μm, ii. 3.0029 μm, iii. 3.0516 μm, iv. 3.0403 μm) and the volume fraction of spherical active particles is about 40% (i. 40.12 %, ii. 39.96 %, iii.40.20 %, iv. 40.00 %). The ratio of additive to binder is 0.3:1. The volume fraction of electrolyte is 35 %. The mean effective conductivities of solid-phase materials of (i), (ii), (iii), and (iv) are 5.077E-6 S/cm, 3.050E-6 S/cm, 1.769E-6 S/cm, and 1.409E-6 S/cm, respectively. (a) Active particle size distribution in 3-D electrode microstructures. (b) Nyquist plot of impedance response in 3D. (c) Magnitude image. (d) Phase angle plot. 28

Figure 11. Dependence of the local bounded impedance response on the mean particle radius effect of imaginary porous electrodes with the different size distribution of spherical active particles. The mean radii of active particles of (i), (ii), and (iii) porous electrodes are 6.504 μm, 4.0188 μm, and 2.0026 μm, respectively. The specific surface area of active particles is 1500 cm^{-1}. The volume fraction of the particles is 35%. Electrical conductivities of electrolyte and solid-phase materials are 5.5E-5 S/cm and 1E-6 S/cm, respectively. (a) Active particle size distribution function. (b) Nyquist image of impedance response. (c) Magnitude image. (d) Phase angle plot 30

Figure 12. Dependence of the local bounded impedance response on the mean particle radius effect of virtual porous electrodes with the active particles of Fig. 8-(a). The specific surface area of active particles is 1500 cm^{-1}. The volume fraction of the particles is 35%, and the ratio of additive to PVDF in the 3D microstructure electrodes is 0.3:1. Electrical conductivities of electrolyte are 5.5E-5 S/cm. The mean radii of active particles of (i), (ii), and (iii) porous electrodes are 6.504 μm, 4.0188 μm, and 2.0026 μm, respectively. The effective conductivities of solid-phase materials of (i), (ii), and (iii) are 1.23833E-6 S/cm, 1.25832E-6 S/cm, and 1.51001E-6 S/cm, respectively. Magnified view of Nyquist image (b) close to origin is shown in image (a). (c) Magnitude image. (d) Phase angle plot.....31

Figure 13. Dependence of the impedance response on the volume fraction of the active materials. Mean radius of spherical active particles is approximately 5 μm (i. 5.074 μm, ii. 5.0017 μm, iii. 5.0196 μm, iv. 5.0158 μm). The ratio of additive to PVDF is 0.3:1. The volume fraction of electrolyte is 35 %. The electrical conductivity of liquid-phase materials is 1.0E-2 S/cm. The specific surface areas of active particles in the electrodes are (i) 1412.3969 cm^{-1}, (ii) 1875.3419 cm^{-1}, (iii) 2343.8790 cm^{-1}, and (iv) 2796.5195 cm^{-1}. The mean effective conductivities of solid-phase materials of (i), (ii), (iii), and (iv) are 1.378E-6 S/cm, 1.661E-6 S/cm, 2.607E-6 S/cm, and 8.265E-6

S/cm, respectively. (a) Active particle size distribution function. Magnified view of Nyquist image (b) close to origin is shown in image (c). (d) Warburg plot of impedance response. (e) Magnitude image. (f) Phase angle plot. 33

Figure 14. The morphology effect of the active material on the impedance response of the imaginary electrodes. The aspect ratios of cylindrical particles(1:γ) and platelet particles(1:α:β) are 1:10 and 1:10:10,respectively. The specific surface area of active particles is 2900 cm^{-1} and the effective conductivity of solid-phase materials is 2E-6 S/cm. The electrolyte conductivity is 5.5E-5 S/cm. (a) The characteristic mean length is 2um. The volume fractions of spherical, cylindrical, and platelet active particles are 20%, 30%, and 60%, respectively. (a1) Active particle size distribution function. (a2) Nyquist image of impedance response. (a3) Bode plots of impedance response. (b) The Sauter mean radius is 2um, and the volume fraction of active particles is 20%. (b1) Active particle size distribution function. (b2) Nyquist image of impedance response. (b3) Bode plots of impedance response. 36

Figure 15. The morphology effect of the active material on the impedance response of the imaginary electrodes. The aspect ratios of cylindrical particles(1:γ) and platelet particles(1:α:β) are 1:10 and 1:10:10,respectively. The specific surface area of active particles is 2900 cm^{-1} and the effective conductivity of solid-phase materials is 2E-6 S/cm. The electrolyte conductivity is 5.5E-5 S/cm. (a) The characteristic mean length is 0.1333335um. The volume fractions of spherical, cylindrical, and platelet active particles are 20%, 30%, and 60%, respectively. (a1) Active particle size distribution function. (a2) Nyquist image of impedance response. (a3) Bode plots of impedance response. (b) The Sauter mean radius is 0.1333335um, and the volume fraction of active particles is 20%. (b1) Active particle size distribution function. (b2) Nyquist image of impedance response. (b3) Bode plots of impedance response. 37

Figure 16. Morphology effect of the active material on the impedance response of the 3-D microstructure electrode. Sauter mean radius is 3um and the volume fraction of active materials is 35%. The specific surface area of active particles is approximately 1900 cm^{-1} (i. 1914.82 cm^{-1}, ii. 1920.72 cm^{-1}, iii. 1885.58 cm^{-1}). The ratio of additive to PVDF is 0.3:1. The volume fraction of electrolyte is 35 %. The effective conductivities of solid-phase materials of (i), (ii), and (iii) are 4.27E-7 S/cm, 2.025E-6 S/cm, and 2.094E-6 S/cm, respectively. 40

Figure 17. Schematic diagram of particle-SEI and SEI-electrolyte interface and an equivalent circuit diagram 42

Figure 18. Schematic diagram of intercalation active particle with solid electrolyte interphase. (a) Spherical particle. (b) Cylindrical Particle. (c) Platelet Particle 44

Figure 19. The effect of SEI on an active spherical particle. Active particle radius is 8 μm. SEI thickness is 0.1 μm. Capacity of SEI film is 1.0E-10 F/cm^2. 46

Figure 20. The effect of SEI film resistance dependent on SEI thickness of an active spherical particle. Active particle radius is 8.5 μm. Capacity of SEI film is 1.0E-11 F/cm^2. 47

Figure 21. The effect of SEI film resistivity and Capacity dependent on SEI thickness of an active spherical particle. Active particle radius is 8.5 μm. 48

Figure 22. The impedance response of the effect of an active spherical particle radius with SEI. SEI thickness is 0.05 μm. 50

Figure 23. The effect of SEI with various morphologies of an active spherical particle. Active particle characteristic length is 8.5 μm. SEI thickness is 0.1 μm. 50

Figure 24. Brittle fracture in cylindrical graphite anode material [90] 51

Figure 25. Random lattice spring method [49] 52

Figure 26. The effect of mechanical degradation by coupling diffusion induced fracture with impedance response of an active spherical particle. The particle radius is 15 μm. (a) Comparison between discharge profiles at 4C with diffusion induced fracture and without it. (b) Nyquist plot at x = 0.304.. 54

Figure 27. The spherical active particle radius effect of mechanical degradation with impedance response. (a) Comparison between discharge profiles at 4C with diffusion induced fracture and without it. Magnified view of Nyquist image (b) at x = 0.595 close to origin is shown in image (c). 55

Figure 28. The image of agglomerate active particles with Sauter mean diameter. R_{s1} and R_{s2} are $4\mu m$ 56

Figure 29. The agglomerate active particle effect of mechanical degradation with impedance response. (a) Comparison between discharge profiles at 4C with diffusion induced fracture and without it. Nyquist image at x = 0.6 is shown in image (b). 58

LIST OF TABLES

Page

Table 1. Material electrical properties for 3D electrode microstructure [83]. 21

Table 2. Physical properties of the active particles for use in porous electrode simulation. 25

Table 3. Capacity of SEI film with various morphologies.....44

Table 4. Electrode parameters for use in single particle simulations with SEI film. 45

CHAPTER I

INTRODUCTION AND LITERATURE REVIEW

Lithium Ion Batteries (LIBs) are being used extensively in vehicular electrification as a reliable source of renewable energy [1]. Because of the very low molecular weight of Li ions, LIBs show very high energy density along with large shelf life. In order to satisfy the ever-growing requirements for LIBs, a great deal of research is being carried out to improve the energy capacity, the power performance, and the calendar life of these batteries. Especially, research concerning the fabrication of electrodes with intercalation particles has been conducted for several decades [2-6]. Porous electrodes have been adopted due to the inherent advantage of high surface area for charge transfer. It leads to increased catalytic activity [7] which is a characteristic of intercalation particles. The relationship between porous composite electrodes and their electroanalytical characteristics has been used to predict and estimate battery performance [8-22].

Furthermore, many researches for degradation have been conducted in order to predict battery life. During the battery operation, the LIB performance decays due to chemical degradation such as the formation of SEI and mechanical degradation such as the form of fracture formation [23, 24]. The formation of SEI layer leads irreversible capacity loss and increase in charge transfer resistance because of SEI film resistance [25-31]. Also, the diffusion induced stress generates multiple micro-cracks inside the electrode active particle [32-35]. These cracks reduce the local diffusivity at multiple

points within the active particle. This reduction in diffusivity results in change of concentration distribution and the increment of diffusion impedance at low frequencies of the active particle.

One of the most powerful methods for electroanalytical characterization to predict these problems is Electrochemical Impedance Spectroscopy (EIS), which measures the rate of individual electrode kinetic steps by calculating the ratio of a small sinusoidal perturbation of potential to its corresponding small sinusoidal perturbation of current [36-40]. EIS is a tool that bridges between diagnostic purpose, which is to characterize changes at a surface under specific system parameters, and application purposes, which is to tailor system in order to obtain a desirable effect on a surface [41]. EIS is widely used as a standard characterization technique of many material systems (such as, corrosion phenomena) and applications (such as, batteries and fuel-cells) [40, 42, 43].

The current state-of-the-art of the LIB impedance analysis doesn't include the influence of the electrode microstructure and active particle morphological heterogeneity on the underlying solid-state transport as well as electronic resistance. Furthermore, the effects of SEI formation and fracture on the solid-state impedance lack details of morphological influence. In this research, a mathematical modeling has been presented in order to rigorously incorporate the influence of electrode microstructure and morphological heterogeneity on the impedance response and concomitant impact on transport behavior and performance.

In this thesis, a mathematical model has been developed to describe the overall electrochemical impedance. This model takes into consideration the dependence on the

interfacial processes and Ohmic drop in the electrode. The effective conductivity of a 3D virtual porous microstructure has also been incorporated within the technique. Three dimensional virtual electrode microstructures consisting of active material, binder, conductive additive and electrolyte have been designed by the technique of Digital Stochastic Modeling (DSM). With this 3D impedance simulation, we test the influence of mean active particle size, active particle size distribution, active particle volume fraction, and effective conductivity on the impedance response of the electrode. Furthermore, we demonstrate the effect of morphology of active materials on diffusion impedance response of the 3D electrode microstructure by using the characteristic diffusion length of active spherical, cylindrical, and platelet particles, and an effective mean particle size. We assumed that the electronic mobility is much faster than the ionic diffusion in the electrolyte because ionic diffusion dominates the transport of charge in various battery materials[44]. Thus, the electrolyte is simply described by a resistor in series with the electrode for impedance analysis.

Furthermore, since aging of dynamic systems is a major concern, finding relevant aging mechanisms is of vital importance. Many efforts have been conducted in order to estimate the life span of battery systems. If the manner in which each component has an effect on battery performance and the chemistry of SEI formation are understood, SEI could be a guideline for improving battery performance [45, 46]. Fracture inside the battery electrode can cause significant amount of reduction in battery life [47-49]. If the pattern of fracture evolution inside the battery electrode is understood, prevention of crack propagation could also improve the battery life [50]. Thus, we focus on the effect

of electrochemical impedance response on the SEI formation of a single intercalation particle and fracture formation inside of a single particle in order to predict battery performance.

These approaches are envisioned to offer a virtual impedance response probing framework to elucidate the influence of electrode microstructural variability and underlying electrochemical and transport interactions.

Electrochemical Impedance Spectroscopy

Electrochemical impedance response is sensitive to the interfacial processes, the surface morphology, and the mass transfer. The electrochemical impedance response of intercalation particle electrodes has been described mathematically by the fundamental physical approach for various electrochemical systems [11, 14, 18, 19, 22, 36, 51-58]. Meyers et. al. have researched the influence of physical properties and particle size distribution in the porous electrode with spherical intercalation particles [36]. Huang et. al. have described the charge transfer at SEI with a mathematical model [53]. Song et. al. have conducted the impact of nanoparticle size distribution and morphology on diffusion impedance [54]. Particularly, in a high energy density battery, interpreting the electrochemical impedance response at very low frequencies – the diffusion impedance – is meaningful for porous composite electrodes [59]. The diffusion impedance of the electrode with small solid-state active materials shows a transition from the Warburg behavior to capacitive behavior due to short diffusion lengths in the active material, which allows diffusion penetration depth to reach the reflective center of the active materials at a low frequency range [60-62]. Since the diffusion impedance with a

reflective boundary depends on diffusion morphology and heterogeneity in active particle size, theoretical formulae of the diffusion impedance have been derived [51, 52, 54, 63].

Chemical and Mechanical Degradation

A protecting solid layer constructed on the negative electrode of Li-ion batteries is the solid electrolyte interphase (SEI) as a consequence of decomposition of electrolyte [26, 64]. It is importance to know the composition and characteristics of SEI because the quality of SEI highly affects battery power performance, cyclability of the battery, exforliation of graphite, irreversible loss of charge and safety [65]. Ramadass et al. have carried out a capacity-fade model which explains a continuous SEI film formation [66]. The paper shows that loss of the active material with continuous cycling was attributed to the formation of a continuous SEI film on the negative electrode surface. The aging mechanism of lithium-ion battery has been reviewed and evaluated by Vetter et al.[67]. The paper suggested that SEI formation and growth leads to an impedance rise at the anode. Huang et al. studied the influence of SEI on impedance response. Increase in the SEI layer thickness leads to an increase of the overall impedance. Hence, this aging aspect is reflected in the impedance [5, 25, 53, 68, 69].

In addition, mechanical degradation in a Li-ion battery electrode can cause significant amount of reduction in battery life [49, 70, 71]. Due to the diffusion process, concentration of Li inside the active particle is not uniform during the lithiation or delithiation process [72]. This difference in Li ion concentration results in the periodic volume change such as swelling or contracting of active particles and stress generation

to achieve mechanical equilibrium within the active particles [24, 73-77]. This diffusion-induced stress causes damage while the battery is in operation. Deviation of species concentration from the equilibrium value induces stress, which can lead to particle fracture [78, 79]. Fracture formation increases the impedance of the battery electrode particle. We will analyze the impedance response of a sing particle by coupling diffusion induced fracture with impedance.

CHAPTER II

MODEL DESCRIPTION

In order to determine the effect of the 3-D microstructure's characteristics on electrochemical impedance response, a multi-tiered modeling approach is used. The modeling approach is a combination of three components: (1) Analytical model for the electrochemical impedance of an effective single particle, (2) the electrochemical impedance of the porous microstructures based on an effective mean particle and a particle distribution function, and (3) stochastic microstructure generation and electrical conductivity evaluation.

Mathematical Model for the Impedance Response of a Single Particle

The starting point for the theoretical description of the impedance response in porous electrode microstructures is a review of the mathematical single particle model that has typically been used in analyzing the electrochemical impedance of porous electrodes for the past several decades [36, 51, 53]. Since the impedance response of a single active particle is affected by the sum of partial current densities, which is equivalent to the total outward current density and potential drop at each position, it is necessary to define these partial current densities. In Figure 1, the total current density of an active particle at interfacial is determined as

$$i_{inf} = i_{dbl} + i_{far} \tag{1}$$

where i_{inf} is interfacial current density, i_{dbl} is the double layer current density (non-faradaic current density), and i_{far} is the faradaic current density. The current density at

the interface can be explained as the sum of non-faradaic and faradaic current densities at the interface.

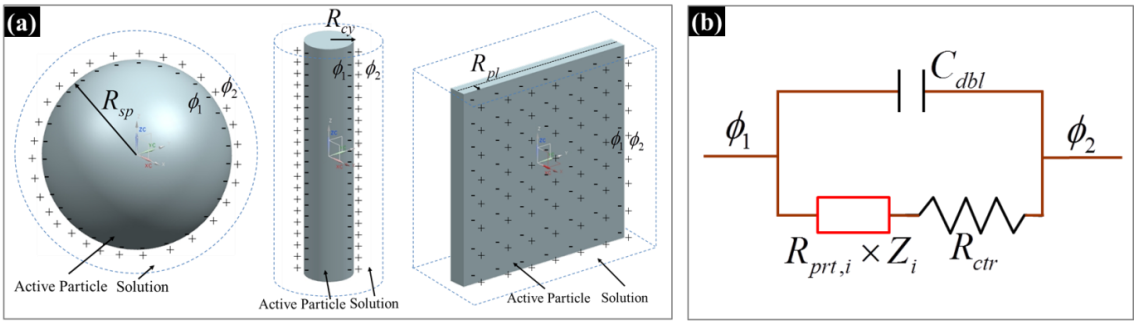

Figure 1. The schematic of the active particles - interfacial impedance with solid-phase diffusion but no insulating film for a single particle; (a) Various morphologies of single active particles, (b) equivalent circuit design

Non-faradaic Impedance

Non-faradaic current, or electric double layer current, does not affect any chemical reactions but involves the accumulation or removal of charges on a single active material particle. This flow, which is always related to capacitive current, is expressed as

$$i_{\mathrm{dbl}} = \mathrm{C}_{\mathrm{dbl}} \frac{\partial(\phi_1 - \phi_2)}{\partial \mathrm{t}} \tag{2}$$

where ϕ_1 and ϕ_2 are the potentials at the interfaces and C_{dbl} is the capacity of the double layer. The impedance for a non-faradaic reaction, the ratio of the potential across the interface to non-faradaic current density in the frequency domain, is defined as

$$Z_{dbl} = \frac{1}{j\omega C_{dbl}} \tag{3}$$

Faradaic Impedance

Chemical reactions occurring at a single particle surface gives rise to a faradaic current density. The correlation between faradaic current density and potential drop across the interface can be explained by Butler-Volmer equation, given as

$$i_{far} = i_0\left(\exp\left[\frac{\alpha_a F}{RT}\left(\phi_1 - \phi_2 - U\right)\right] - exp\left[-\frac{\alpha_c F}{RT}\left(\phi_1 - \phi_2 - U\right)\right]\right) \tag{4}$$

where $\alpha_a + \alpha_c = 1$, α_a is transfer coefficient of the anodic, α_c is transfer coefficient of the cathodic, i_0 is the exchange current density, and U is the open circuit potential of the charge transfer reactions. In order to calculate the faradaic impedance response of a single active particle, the linearized current density equation expressed as a function of the potential and the surface concentrations is needed. The linearized Butler-Volmer equation in the frequency domain is defined as [36]

$$\tilde{i}_{far} = \frac{F\left(\alpha_a + \alpha_c\right)i_0}{RT}\left[\tilde{\phi}_1 - \tilde{\phi}_2 - \frac{\partial U}{\partial c_i}\tilde{c}_i\left(R_i\right)\right] \tag{5}$$

where c_i is the concentration of intercalation ions in a single particle, i indicates particle geometries such as sp (sphere), cy (cylinder) and pl (platelet), and $\tilde{c}_i\left(R_i\right)$ is the surface concentration of a single particle. To describe the faradaic impedance, we need to focus on the surface concentration of an active material particle.

In this mathematical single particle model, the mobility of electrons is assumed to be much quicker than that of the intercalating ions in an active particle [44], and therefore formation of local charge neutrality is given in the system. Because of this condition, the mass balance of lithium ions in an intercalation particle of active material

is governed by ionic diffusion, which can be described by Fick's second law in various coordinate systems. The diffusion equation in the time domain is defined as

$$\frac{\partial c_i(r,t)}{\partial t} = D_a \nabla^2 c_i(r,t) \tag{6}$$

where r is the distance from the symmetric center of the spherical, cylindrical, and platelet active material particles, t is the time variable, and D_a is the diffusion coefficient of the active material.

Let us consider the diffusion equations with various morphologies in the frequency domain. Then the following ordinary differential equations are obtained:

$$jw\tilde{c}_{sp} = \frac{D_a}{r^2}\frac{d}{dr}\left(r^2 \frac{d\tilde{c}_{sp}}{dr}\right)$$

$$jw\tilde{c}_{cy} = \frac{D_a}{r}\frac{d}{dr}\left(r \frac{d\tilde{c}_{cy}}{dr}\right)$$

$$jw\tilde{c}_{pl} = D_a \frac{d}{dr}\left(\frac{d\tilde{c}_{pl}}{dr}\right) \tag{7}$$

The symmetry at the center of a single particle and Faraday's law at the interface are used as boundary conditions, where

$$\frac{d\tilde{c}_i}{dr} = 0 \qquad at \;\; r = 0$$

$$-D_a \frac{d\tilde{c}_i}{dr} = \frac{\tilde{i}_{far}}{F} \qquad at \;\; r = R_i \tag{8}$$

The analytical solutions of these differential equations with the boundary conditions are given in Eq. 9.

$$\tilde{c}_{sp} = \frac{\tilde{i}_{far} R_{sp}^2}{F D_a} \left(\frac{1}{\sin\left(\sqrt{-\frac{j\omega}{D_a}} R_{sp}\right) - \sqrt{-\frac{j\omega}{D_a}} R_{sp} \cos\left(\sqrt{-\frac{j\omega}{D_a}} R_{sp}\right)} \right) \frac{\sin\left(\sqrt{-\frac{j\omega}{D_a}} r\right)}{r}$$

$$\tilde{c}_{cy} = -\frac{\tilde{i}_{far}}{F D_a \sqrt{\frac{j\omega}{D_a}}} \frac{I_0\left(\sqrt{\frac{j\omega}{D_a}} r\right)}{I_1\left(\sqrt{\frac{j\omega}{D_a}} R_{cy}\right)}$$

$$\tilde{c}_{pl} = -\frac{\tilde{i}_{far}}{F D_a \sqrt{\frac{j\omega}{D_a}}} \left(\frac{e^{\sqrt{\frac{j\omega}{D_a}} r} + e^{-\sqrt{\frac{j\omega}{D_a}} r}}{e^{\sqrt{\frac{j\omega}{D_a}} R_{pl}} - e^{-\sqrt{\frac{j\omega}{D_a}} R_{pl}}} \right) \tag{9}$$

Thus, the transfer functions between the surface concentration of an intercalation particle and the faradaic current density can be specified as

$$Z_{sp} = -\frac{F D_a \tilde{c}_{sp}\left(R_{sp}\right)}{\tilde{i}_{far} R_{sp}} = \frac{\tanh\left(R_{sp}\sqrt{\frac{j\omega}{D_a}}\right)}{R_{sp}\sqrt{\frac{j\omega}{D_a}} - \tanh\left(R_{sp}\sqrt{\frac{j\omega}{D_a}}\right)}$$

$$Z_{cy} = -\frac{F D_a \tilde{c}_{cy}\left(R_{cy}\right)}{\tilde{i}_{far} R_{cy}} = \frac{I_0\left(R_{cy}\sqrt{\frac{j\omega}{D_a}}\right)}{R_{cy}\sqrt{\frac{j\omega}{D_a}} I_1\left(R_{cy}\sqrt{\frac{j\omega}{D_a}}\right)}$$

$$Z_{pl} = -\frac{F D_a \tilde{c}_{pl}\left(R_{pl}\right)}{\tilde{i}_{far} R_{pl}} = \left(\frac{e^{R_{pl}\sqrt{\frac{j\omega}{D_a}}} + e^{-R_{pl}\sqrt{\frac{j\omega}{D_a}}}}{e^{R_{pl}\sqrt{\frac{j\omega}{D_a}}} - e^{-R_{pl}\sqrt{\frac{j\omega}{D_a}}}} \right) \frac{1}{R_{pl}\sqrt{\frac{j\omega}{D_a}}} \tag{10}$$

where Z_{sp}, Z_{cy}, and Z_{pl} indicate the local bounded diffusion impedance of a spherical, cylindrical, and flat single particle, respectively. The impedance for a faradaic reaction can be expressed by inserting the local bounded diffusion impedance (Eq.10) into the linearization of the Butler-Volmer equation (Eq. 5).

$$Z_{\mathrm{far,i}} = \frac{\tilde{\phi}_1 - \tilde{\phi}_2}{\tilde{i}_{far}} = R_{ctr} + R_{prt} \times Z_i \tag{11}$$

$$\text{where } R_{ctr} = \frac{RT}{F\left(\alpha_a + \alpha_c\right) i_0}, \; R_{prt} = \left(-\frac{\partial U}{\partial c_i} \right) \frac{R_i}{F D_a} \tag{12}$$

The faradaic impedance from (Eq.11) and (Eq.12) is composed of two impedance components. The first term manifests the charge transfer impedance which is a non-ohmic resistance related to the kinetics of the charge transfer reaction, and the second reveals the concentration impedance defined by the partial derivative of the open circuit potential with respect to concentration, diffusion coefficient, diffusion length, and diffusion impedance.

Figure 2 shows the effect of the diffusion morphology on diffusion impedance by using local bounded diffusion impedance of the spherical, the cylindrical, and the platelet single particle. The Nyquist image shows a Warbug behavior as high frequency regime because the diffusion length is longer than the penetration depth. This trend is similar to semi-infinite diffusion phenomenon. On the other hand, a capacitive regime is defined at very low frequency. Drawing a vertical line in the Nyquist plot stands for a capacitive regime because the penetration depth goes beyond the limits of diffusion length, and perturbation pilots the active particle to effectively fill up and empty like a

capacitor. There is another different behavior dependent on morphologies. A spherical active particle shows small diffusion resistance because the higher ratio of the effective surface to volume is easier to diffuse throughout the entire domain of the active particle.

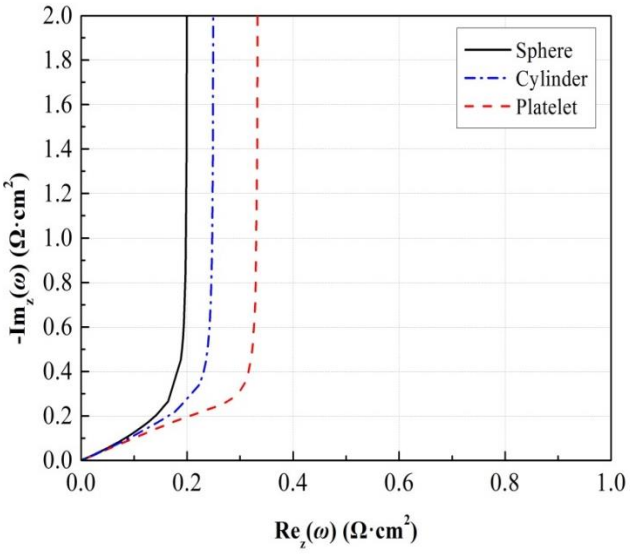

Figure 2. Local bounded diffusion impedance for various particle morphologies.

Impedance of an Effective Single Particle

An active material without an insulating film is considered in this chapter. We will discuss the film effect at chapter 4. Thus, charging processes of the electrochemical double layer and faradaic reaction only affect the total impedance response. From Figure 1 with faradaic and non-faradaic impedances, the total impedance of a single active particle can be explained as

$$Z_{total,i} = \frac{Z_{far,i} Z_{dlb}}{Z_{far,i} + Z_{dlb}} \tag{13}$$

Figure 3 explains the effect of impedance response on the active particle radius. At low frequency regime, there is only different behavior because of the various diffusion lengths. The diffusion resistance of an active particle decreases with decreasing an active particle radius. This is due to the fact that a smaller particle means a more curved morphology. At high frequency, we can see the charge transfer impedance behavior like semicircle which results from the combination between charge transfer resistance and electric double layer capacitance. At the high frequency, the perturbation wave could not penetrate inside the active particle for scanning the internal dynamics of a system. That's why the figure shows the interfacial impedance as the semicircle at high frequency in Figure 3.

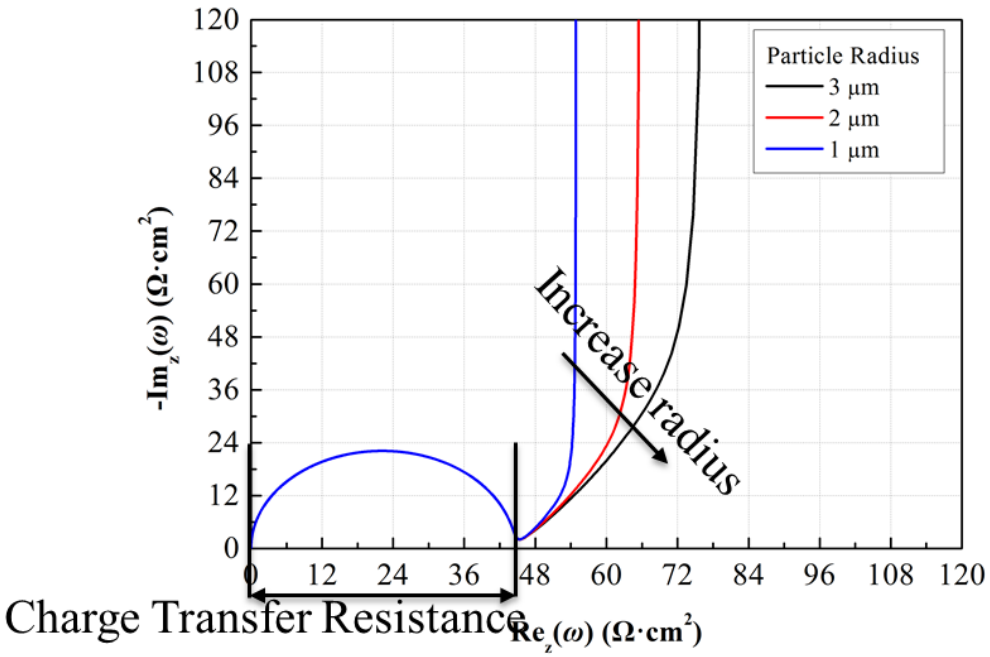

Figure 3. Nyquist plot of impedance of a single particle for interfacial impedance with solid-phase diffusion limitations but no insulating film

Impedance of 3-D Electrode Microstructure

Since we have determined the effective electrical conductivities of the generated electrode models and the impedance response of a single active particle, we are able to couple these properties with a designed 3-D microstructure by using a particle-size distribution function for the impedance response.

Particle Size Distribution and Sauter Mean Diameter

Before considering the particle size distribution, we need to know the morphology of the active particles. The existent active particles in the actual micro-electrode have various kinds of structures such as spherical, cylindrical, flat, and agglomerate. According to (Eq. 10), we know that the morphology of the active particle can determine the response of the local bounded diffusion impedance; hence the equivalent characteristics description of an amorphous active particle is needed for solving the impedance response in the analytical approach.

The concept of the Sauter mean diameter or surface mean diameter is widely used in the field where the effective surface area is of most interest, such as in reaction and absorption research [80]. Figure 4 (a) shows the relationship between an agglomerate particle and a Sauter mean particle. Sauter mean diameter is the diameter of a sphere that has the same ratio of volume to active surface area and can characterize the particles with different shapes, which is given by:

$$d_{smd} = 6 \cdot \frac{V_P}{A_P} \tag{14}$$

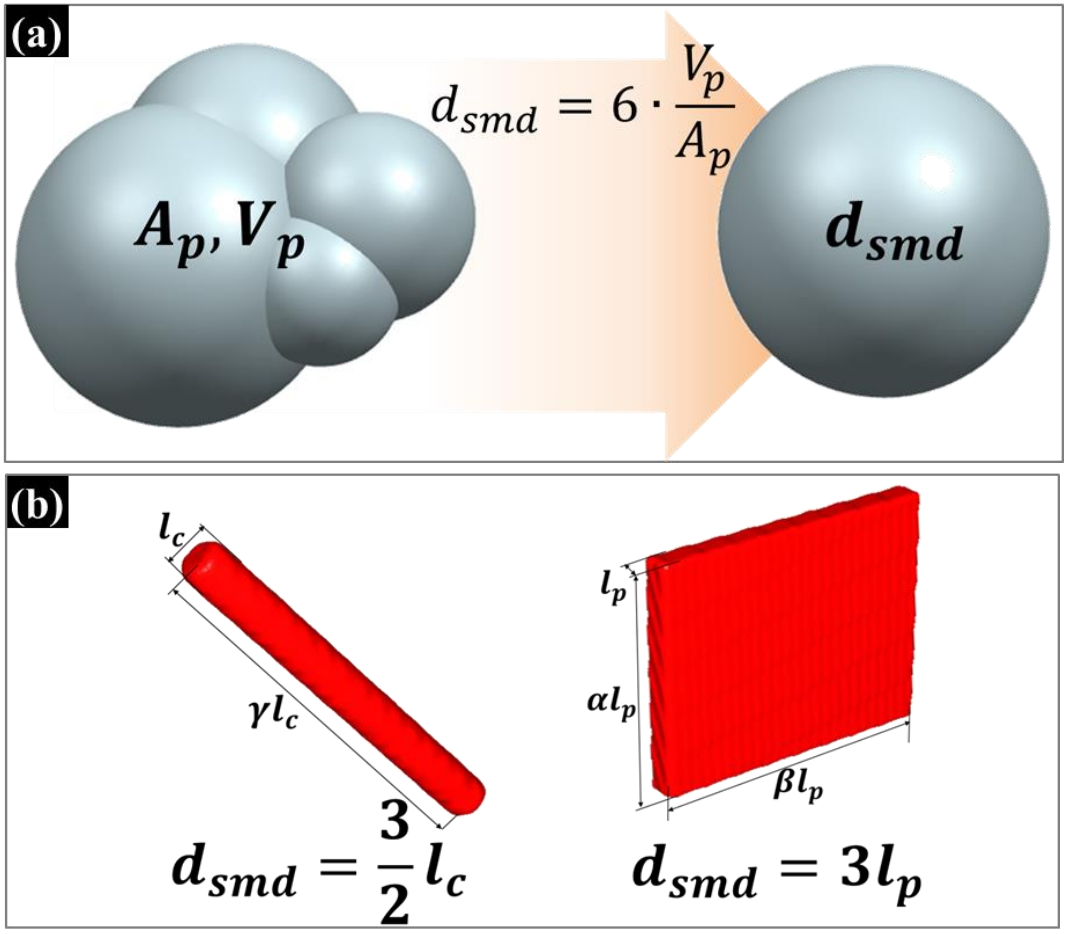

Figure 4. The diameter design of a sphere that has the same ratio of particle volume to effective surface area as a particle of interest; (a) The relation between an amorphous particle and a sauter mean particle. A_p and V_p are the effective surface area and the particle volume, respectively. (b) The sauter mean diameters of a cylindrical particle and a platelet particle. α, β, and γ are aspect constants

where d_{smd} is the Sauter mean diameter, V_p is the volume of the particle of interest, and A_p is the effective surface area of the designated particle of interest. The Sauter mean diameters of a cylindrical particle and a platelet particle are considered in Figure 4 (b) in order to analyze the diffusional impedance effect dependent on the Sauter mean diameter.

The effective surface areas of a spherical active particle, a cylindrical active particle, and a platelet active particle can be defined as πd_{sp}^2, $\pi l_{cy} \cdot \gamma l_{cy}$, and $2 \cdot (\alpha l_{pl} \cdot \beta l_{pl})$, respectively, where α and β are the aspect ratios of the side lengths of the platelets, and γ is the aspect ratio of the height of the cylinders. The Sauter mean diameters of the cylinder and platelet are expressed by:

$$d_{smd,cy} = \frac{3}{2} l_{cy}$$

$$d_{smd,pl} = 3 l_{pl} \tag{15}$$

Based on the Sauter mean diameter, the Gaussian distribution in the logarithm of the particle is employed in order to define the distribution of particles with various geometries, which is given by:

$$N_i(r_{smd,i}) dr_{smd,i} = \frac{1}{NR_i} \left[\frac{a_{smd,i}^3 e^{-\left(\frac{\psi}{4}\right)^2}}{(4\pi) 9 \varepsilon_{smd,i}^2 \sqrt{\pi} \psi} \right] \exp \left[- \left(\frac{\ln\left(\frac{r_{smd,i} a_{smd,i}}{3\varepsilon_{smd,i}} \right)}{\psi} \right)^2 - \frac{5}{2} \ln\left(\frac{r_{smd,i} a_{smd,i}}{3\varepsilon_{smd,i}} \right) \right] \frac{dr_{smd,i}}{r_{smd,i}} \tag{16}$$

where $N_i(r_i)$ is the number of active material particles per unit electrode volume with distance r_i from the symmetric center of the active particles, and $r_{smd,i}$ is the Sauter mean radius. NR_i is the particle number ratio of the volume of the active particle with the equivalent Sauter mean radius to the Sauter mean particle for shape conversion. For example, NR_{cy} at 1:10 aspect ratio is about 4.444444, and NR_{pl} at 1:10:10 aspect ratio is about 7.0735545.

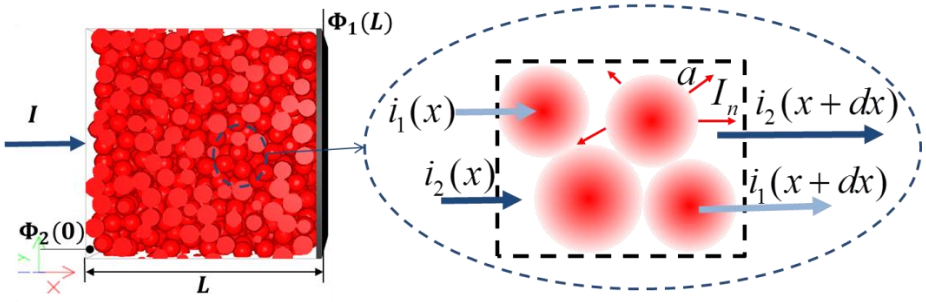

Figure 5. The balance diagram on the fraction of total current flowing

Figure 5 represents the porous electrode of the microstructure consisting of particles with various geometries. As the current passes through the interface of the active particle, it can proceed from the solution phase material to the solid phase material as it moves through the porous microstructure in both the solution phase and the solid phase.

$$\frac{\partial \hat{i}_2}{\partial x} = \sum_{i=geometry} \left[\int_0^{\infty} \left\{ N_i(r_i) A_i(r_i) / Z_{total,i}(r_i) \right\} dr_i \right] (\hat{\Phi}_1 - \hat{\Phi}_2) \tag{17}$$

where $A_i(r_i)$ is the effective surface area at a specific r_j. The total interfacial admittance per unit volume of electrode with various morphological active particles can be defined as

$$\begin{aligned} \overline{AY_t} &= \sum_{i=geometry} \left[\int_0^{\infty} \left\{ N_i(r_i) A_i(r_i) / Z_{total,i}(r_i) \right\} dr_i \right] \\ &= N_{total} \left[\int_0^{\infty} \left\{ P_{sp}(r_{sp}) A_{sp}(r_{sp}) / Z_{total,sp}(r_{sp}) \right\} dr_{sp} + \int_0^{\infty} \left\{ P_{cy}(r_{cy}) A_{cy}(r_{cy}) / Z_{total,cy}(r_{cy}) \right\} dr_{cy} \right. \\ &\quad \left. + \int_0^{\infty} \left\{ P_{pl}(r_{pl}) A_{pl}(r_{pl}) / Z_{total,pl}(r_{pl}) \right\} dr_{pl} \right] \end{aligned} \tag{18}$$

where $A_i(r_i)$ is the effective surface area at a specific r_j, N_{total} is the number of total active particles per unit electrode volume. $P_i(r_i)$ is the probability density function with the distance r_i from the symmetric center of the active particles. Meyers *et al.* [36] provided that the entire impedance of the porous electrode microstructure can be described as

$$Z_{EM} = \frac{L}{\kappa + \sigma}\left[1 + \frac{2 + \left(\frac{\sigma}{\kappa} + \frac{\kappa}{\sigma}\right)\cosh(\nu)}{\nu \sinh(\nu)}\right] \tag{19}$$

$$\text{where} \quad \nu = L\left(\frac{\kappa + \sigma}{\kappa\sigma}\right)^{1/2}\left(\overline{AY_t}\right)^{1/2} \tag{20}$$

σ is solid-phase electrical conductivity, and κ is the electrolyte electrical conductivity. The electrical conductivity of solid phase comes from the electrical conductivity evaluation of the stochastic microstructure generation which is composed of the active material, the additive, and the binder. This explains the impact of solid-phase and electrolyte ohmic resistances on impedance distribution of 3-D electrode microstructures.

Stochastic Microstructure Generation and Electrical Conductivity Evaluation

Stochastic Generation of Electrode Microstructure

3-D porous microstructure can be generated by using the technique of digitally stochastic models. This randomly structured micro-model is based on specified statistical information such as particle size distribution and porosity. These design parameters of the model from the statistical information determine the characteristics of the microstructure including effective electrical conductivity. The stochastic modeling

technique is based on the idea that a representative 3D structure can be designed by the intrinsic arbitrary phase function. The generated models, which are due to the randomness of the real structures, are not exactly the same geometric structure but are fitted by choosing parameters so that the characteristic properties of the material are realistically represented [81]. Stochastic modeling allows for a random distribution of objects within the generated structures and includes the macroscopic homogeneity present in the actual structures.

Effective Electrical Conductivity

The electrode fabrications process is illustrated in Figure 6. Table 1 shows the electrical properties of each material such as active material, additive, binder, and electrolyte. Spherical, cylindrical, and platelet active particles are modeled in each set of this paper. The properties of LiNi0.8Co0.15Al0.05O2 were considered to create the active particles. In order to generate active particles with various geometries, the logarithm Gaussian distribution of the particle is employed for particle size distribution.

Conductive additives like thin spherical disks with aspect ratios b/a, c/a, and c/b set to 7.4, 7.4, and 1 are modeled as shown in Figure 7, respectively [82]. The binder is inserted into the generated electrodes which constructed of active particles and conductive additive materials in spaces where two or more particles were close together. An electrolyte of liquid phase is filled in the remaining void space. The representative volume for computational domain was considered to 50 µm × 50 µm × 50 µm, with a voxel size of 0.25 µm. The electrode microstructures were generated using voxel-based modeling.

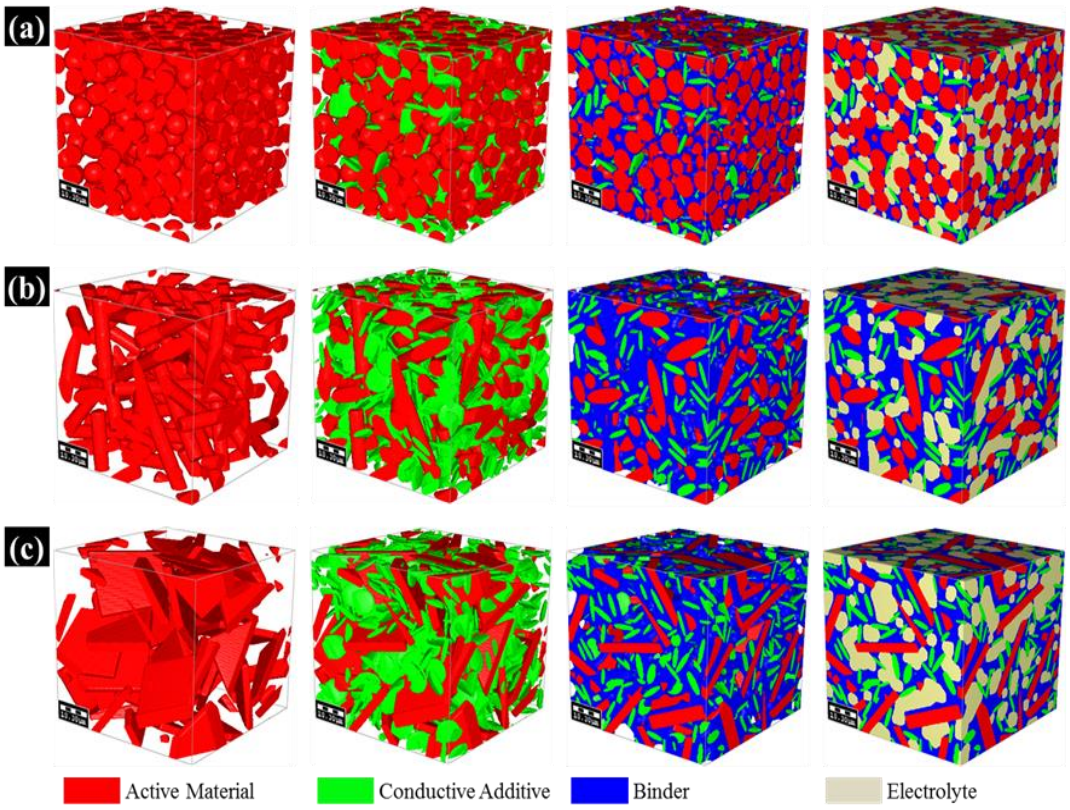

Figure 6. Full 3D microstructure electrode model with (a) Spherical active particles (b) Cylindrical active particles (c) Platelet active particles

Table 1. Material electrical properties for 3D electrode microstructure[83].

Materials	Electrical Conductivity(S/m)
LiNi0.8Co0.15Al0.05O2	0.04
Conductive Additive	10000
Binder	1.0E-13

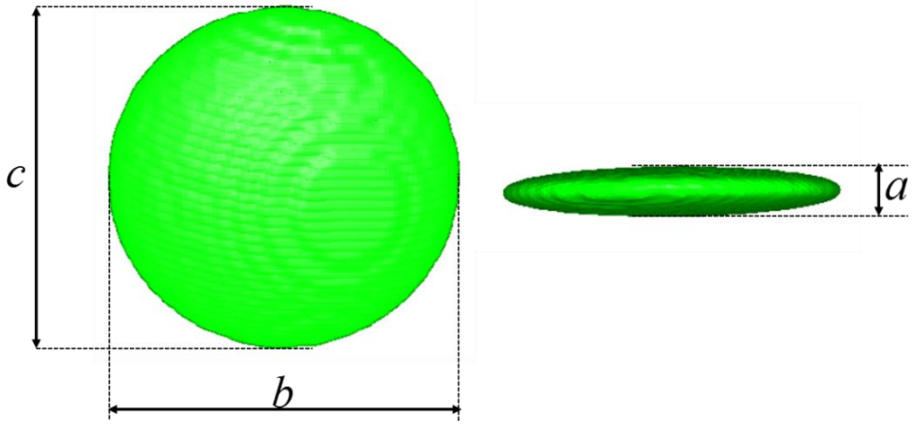

Figure 7. Schematic of conductive additive

The three dimensional stationary conduction equation is solved for determining the effective conductivity of multi-component porous electrode. This stationary conduction equation can be defined as:

$$\nabla\left(\sigma_L \nabla V\right) = \dot{I} \qquad in\ \Phi_D \tag{21}$$

where Φ_D is the domain under consideration, $\dot{I}$ is a source term, V is a potential, and σ_L is a local electrical conductivity. The equation is solved using a combination of FFT and BiCGStab methods, and is carried out in the GeoDict simulation, which generate the 3D microstructure and evaluate the electrical effective conductivities.

The coefficient of variation (CV) can be estimated of the deviation of an effective electrical property on an entire electrode system with heterogeneous particles. CV can be defined as the following.

$$CV = \frac{\sigma_{CV}}{\mu_{CV}} \tag{22}$$

where μ_{CV} is the arithmetic mean of effective conductivity and σ_{CV} is the standard deviation of effective conductivity on an microstructure. A CV below 0.5 expresses homogeneity, with a value greater than 1 expressing extremely heterogeneity [84]. To evaluate that deviation of random structure generation does not have a large influence on the generated microstructures, the CV was calculated with 5 samples for each of the evaluated microstructures. As shown in Figure 8, the CV remained under 0.65 for each electrode that was evaluated.

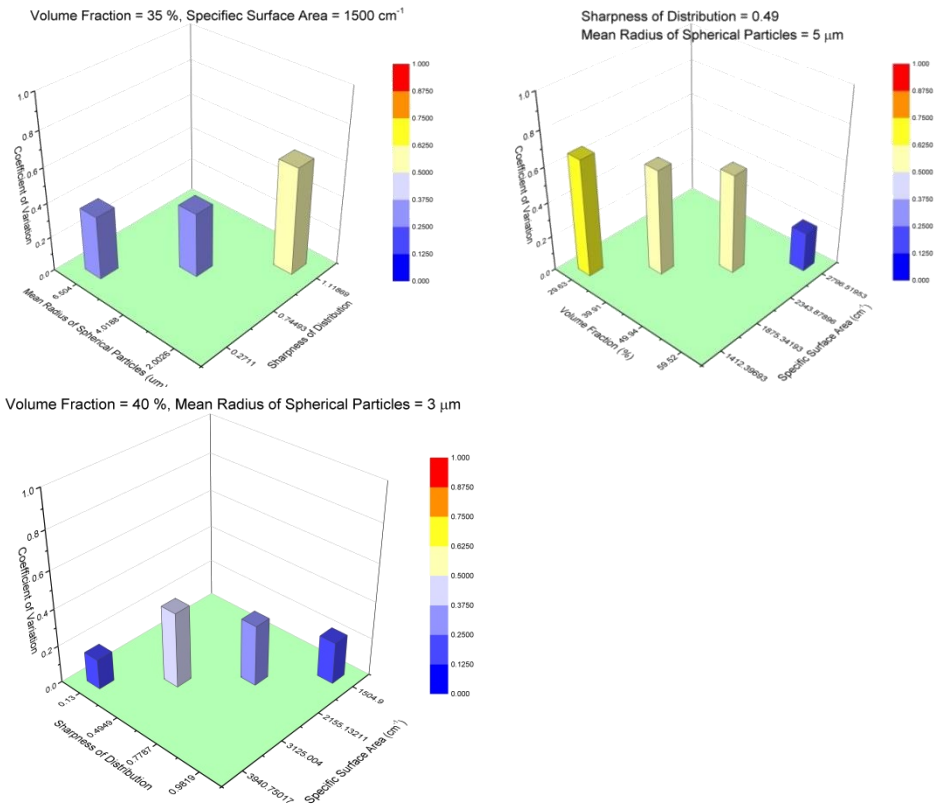

Figure 8. The coefficient of variation for evaluated electrode microstructures**.**

CHAPTER III

ANALYSIS OF THE EFFECT OF MICROSTRUCTURES ON THE IMPEDANCE RESPONSE

Influence of Porous Electrode Microstructure on the Impedance Response

The simulated impedance response of the microstructure electrode is illustrated in Figure 9 as a function of the effective electrical conductivity of the porous electrode. Electrode parameters for use in porous electrode simulation are shown in Table 2. Data is presented in the Nyquist format in Figure 9 (b) over a wide frequency range of 10^{6} to 10^{-6} Hz. The same structure of spherical active particles of about 3um mean radius is used for all micro-electrodes in Figure 9 (a). (i), (ii), and (iii) microstructures are considered in Figure 9, to examine the effect of changing the effective conductivity of the electrode in solid phase by altering the ratio of additive to binder. (iii), (iv), (v), and (vi) microstructures in the figure illustrate the effect of changing the liquid phase effective conductivity by considering electrolytes with various electrical conductivities. Since the active particles in these porous microstructures are designed by using identical properties, these results explains that the electrical conductivity changes of the solid phase and liquid phase impact high frequency impedance data as well as the lower frequency impedance information [51]. An adequate composition of insertion materials such as active material, additive, and binder can lead to a decrease in overall impedance due to resulting changes in the solid phase electrical conductivity, but an inadequate

composition leads to deficient effective conductivity in the porous electrode. In addition, since the ratio of electrical conductivities of the electrolyte and solid phase affects the

Table 2. Physical properties of the active particles for use in porous electrode simulation**.**

Property	Value
i_0	0.69 x 10^{-3} A/cm^2
T	353.15 K
$\alpha_a + \alpha_c$	1
$-\frac{\partial U}{\partial C_i}$	20.27 V cm^3/mol
C_{dbl}	1 x 10^{-5} F/cm^2
D_a	1.0 x 10^{-9} cm^2/s

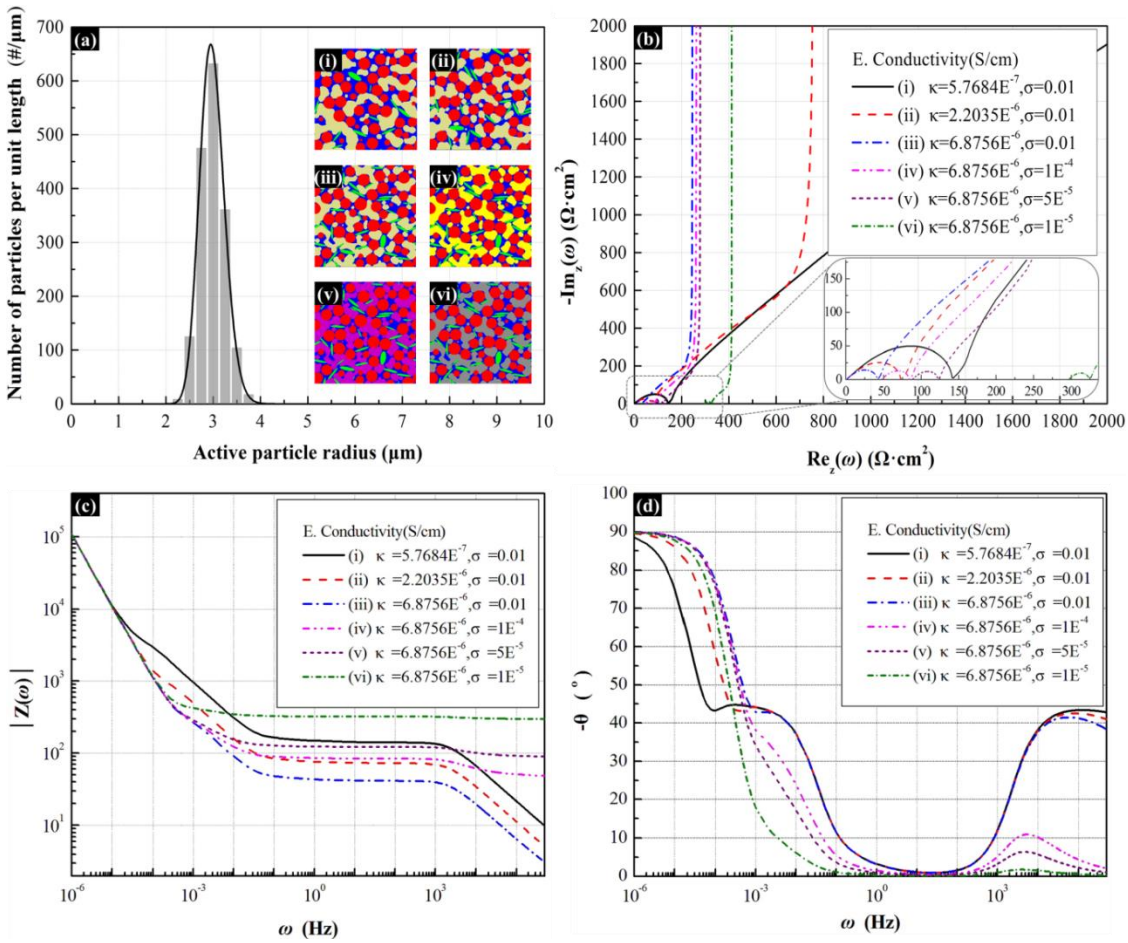

Figure 9. Dependence of the local bounded impedance response on the electrical conductivity of 3D porous electrodes. The mean radius of spherical active particles is 2.9823um and the volume fraction of spherical active particles is 39.19%. The specific surface area is 3883.02cm-1. The volume fraction of electrolyte is 35 %. (a) Active particle size distribution and 3D microstructures with various combinations of electrolyte, binder, and additive. The ratio of additive to binder and the conductivities of electrolyte(S/cm) are (i) 0.101:1, 0.01, (ii) 0.2:1, 0.01, (iii) 0.324:1, 0.01, (iv) 0.324:1, 0.0001, (v) 0.324:1, 0.00005, and (vi) 0.324:1, 0.00001, respectively. (b) Nyquist plot of impedance response in 3D electrodes. (c) Magnitude image. (d) Phase angle plot.

uniformity of the reaction rate in porous electrodes, the impedance response in Figure 9 (b) shows a minimum in passing length before transitioning to capacitive behavior when the ratio of conductivities approaches unity [2]. However, when the ratio of electrical conductivities becomes orders of magnitude greater than unity, such as in the (i), (ii), and (iii) microstructures, the effect of solid conductivity on observed phase angle in the Warburg impedance frequency range becomes less relevant, as shown in Figure 9 (d), and therefore size distribution effect is more easily observed. In addition, when both solid phase electrical conductivity and electrolyte electrical conductivity are low, the significant shift of a curve along the real axis is shown in (vi) microstructure of Figure 9 (b), like Ohmic behavior at high frequencies.

Variation in the specific surface area of active materials, which plays a critical role in interfacial impedances, is often used to understand the impedance response of the electrode. To analyze the effect of electroactive surface area on the impedance response of the porous electrode, various distributions of active particle size, and microstructures with these distributions, are considered in Figure 10 (a). Nyquist, magnitude, and phase angle images, shown in Figure 10 (b), (c), and (d), explain electrochemical impedance behaviors related to the specific surface area of active materials. When the electrode has a narrow size distribution of active particles at the same volume fraction, the effective surface area between active particles and electrolytes becomes large, counteracting slow electrochemical reactions and resulting in high double-layer capacitances. The microstructure electrode therefore has lower lithium-ion transport resistance and the semicircle radius on the Nyquist plot decreases with increase of the electroactive surface

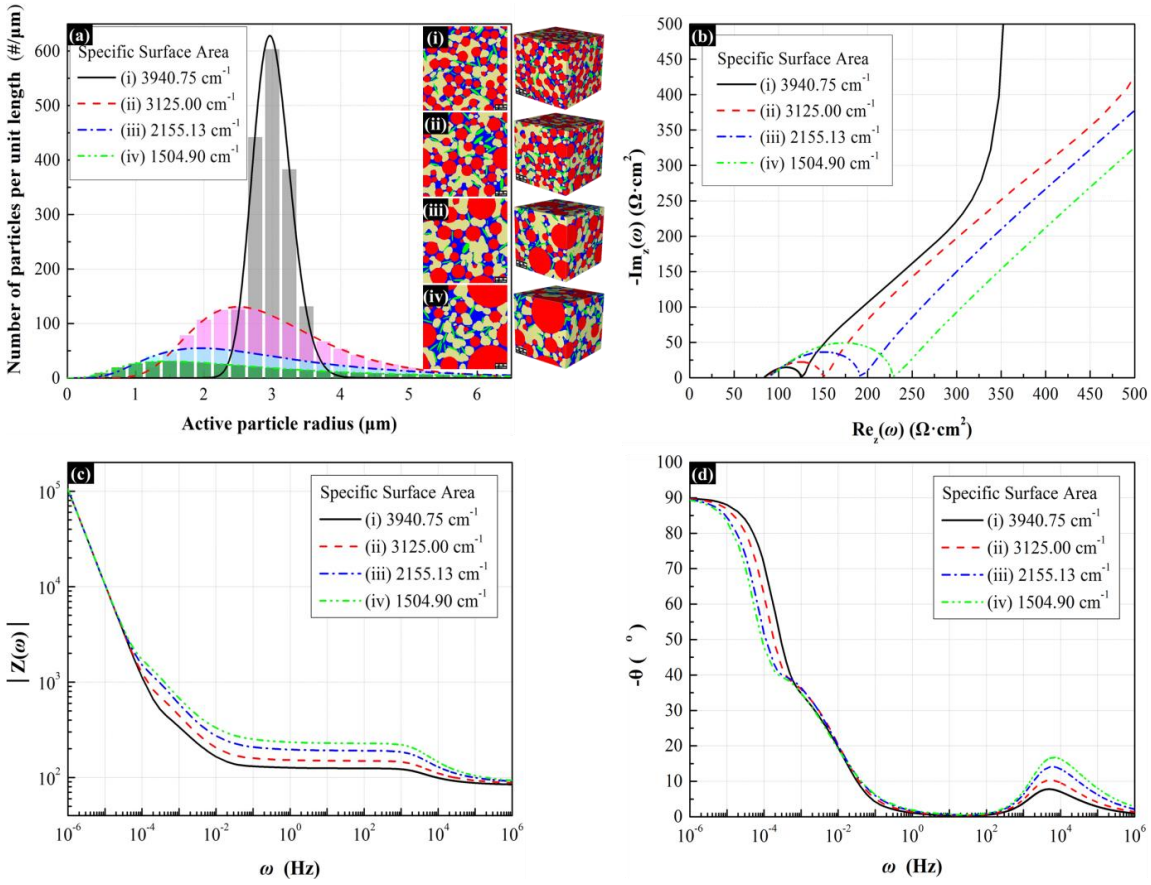

Figure 10. Effect of the specific surface area of active materials on the impedance response of the 3-D microstructure electrode. The mean radius of spherical active particles is approximately 3 μm (i. 3.0031 μm, ii. 3.0029 μm, iii. 3.0516 μm, iv. 3.0403 μm) and the volume fraction of spherical active particles is about 40% (i. 40.12 %, ii. 39.96 %, iii.40.20 %, iv. 40.00 %). The ratio of additive to binder is 0.3:1. The volume fraction of electrolyte is 35 %. The mean effective conductivities of solid-phase materials of (i), (ii), (iii), and (iv) are 5.077E-6 S/cm, 3.050E-6 S/cm, 1.769E-6 S/cm, and 1.409E-6 S/cm, respectively. (a) Active particle size distribution in 3-D electrode microstructures. (b) Nyquist plot of impedance response in 3D. (c) Magnitude image. (d) Phase angle plot.

area of active materials as shown in Figure 10 (b). With the morphology of the active material held constant, the particle size distribution has an effect only on the solid-state diffusion impedance response. Heterogeneity in active particle size, on the other hand, results in various diffusion lengths and therefore affects the low frequency impedance [53]. Thus, at low frequency ranges, specifically the diffusion impedance of the electrode, phase angle image shows a variation solely due to the different size distributions of active particles as depicted in Figure 10 (d).

In order to better examine the effect of heterogeneity in active particle size on diffusion impedance, imaginary porous electrodes with various mean particle radii are created, as shown in Figure 11 (a). These electrodes all have the same specific surface area. Solid phase electrical conductivity and liquid phase electrical conductivity in all electrodes are set to 0.01 S/cm and 1E-6 S/cm, respectively, to eliminate any variations due to the previously-mentioned conductivity ratio effect. The size of the distorted semicircles in Figure 11 (b) is the same because the semicircles represent the charge transfer and double layer impedances, which are influenced by overall surface area of the active materials but not particle size distribution. At lower frequencies, the deviation due to heterogeneous particle size results in variation of the local diffusion impedance, as shown in the Nyquist image. This plot draws a vertical line at low frequencies because the reflective diffusion boundary in each active particle makes a blocking condition. Diard et al. have derived theoretical expressions that show how the diffusion impedance always displays capacitive behavior as the frequency moves towards zero [85].

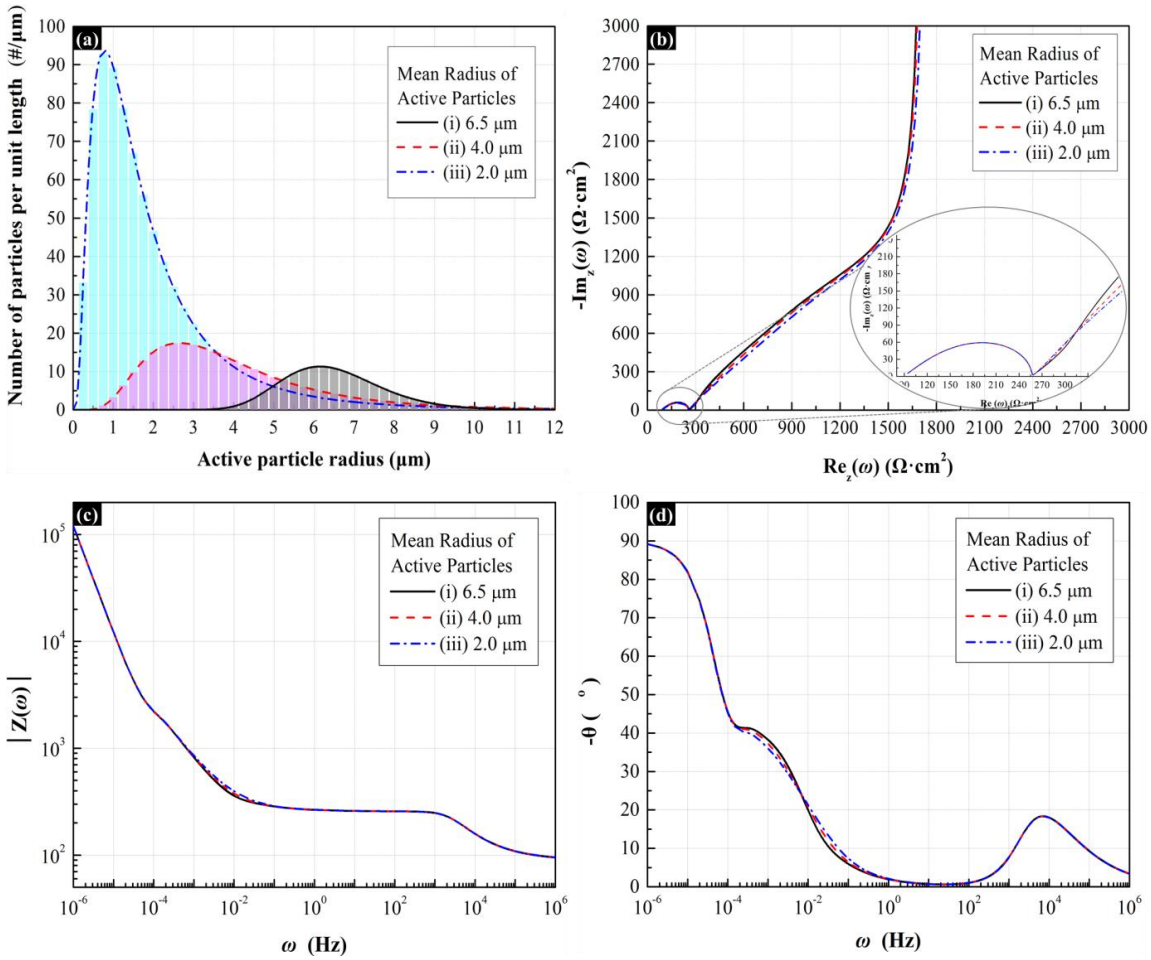

Figure 11. Dependence of the local bounded impedance response on the mean particle radius effect of imaginary porous electrodes with the different size distribution of spherical active particles. The mean radii of active particles of (i), (ii), and (iii) porous electrodes are 6.504 μm, 4.0188 μm, and 2.0026 μm, respectively. The specific surface area of active particles is 1500 cm^{-1}. The volume fraction of the particles is 35%. Electrical conductivities of electrolyte and solid-phase materials are 5.5E-5 S/cm and 1E-6 S/cm, respectively. (a) Active particle size distribution function. (b) Nyquist image of impedance response. (c) Magnitude image. (d) Phase angle plot

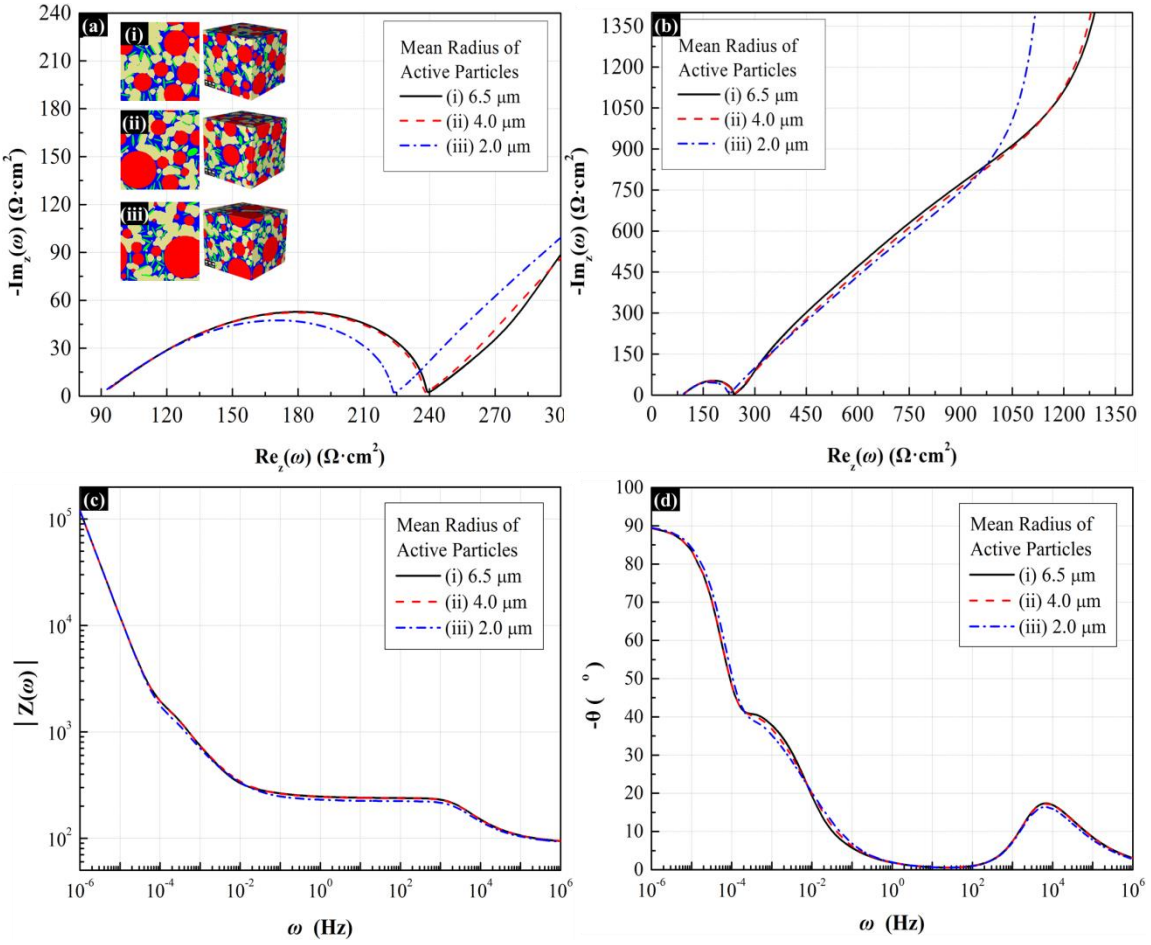

Figure 12. Dependence of the local bounded impedance response on the mean particle radius effect of virtual porous electrodes with the active particles of Fig. 8-(a). The specific surface area of active particles is 1500 cm^{-1}. The volume fraction of the particles is 35%, and the ratio of additive to PVDF in the 3D microstructure electrodes is 0.3:1. Electrical conductivities of electrolyte are 5.5E-5 S/cm. The mean radii of active particles of (i), (ii), and (iii) porous electrodes are 6.504 μm, 4.0188 μm, and 2.0026 μm, respectively. The effective conductivities of solid-phase materials of (i), (ii), and (iii) are 1.23833E-6 S/cm, 1.25832E-6 S/cm, and 1.51001E-6 S/cm, respectively. Magnified view of Nyquist image (b) close to origin is shown in image (a). (c) Magnitude image. (d) Phase angle plot

The impedance response, dependent on both heterogeneity in active particle size and effective electrical conductivity, is demonstrated in Figure 12. 3-D microstructures are designed in Figure 12 (a) - (i), (ii), (iii) by using the active particle size distribution of Figure 11 (a). The semicircles in Figure 12 (a) are different in size – despite the same specific surface area of active materials - which affects charge transfer and double layer impedance. Since a smaller mean radius of spherical particles at the same volume fraction results in more space available between particles, better alignment of electrical paths is observed, and electrical conductivity increases. Smaller electrical conductivity of solid phase makes the semicircle more prominent as discussed in Figure 9. Therefore, as shown in Figure 12 (a), the electrode microstructure (i) with a larger mean radius of spherical particles displays an impedance loop of smaller size in the high frequency domain.

The bulk electrical conductivity of the microstructure electrode - dependent on the volume fraction of active materials - is now used to understand the impedance response of the electrode, as shown in Figure 13. When the amount of active material in the electrode decreases, surfaces of active materials become a small fraction of the overall surface area. In this composition range, there will be plenty of free binder to cover the active material, due to the high overall content of binder. Although adhesion is better with more binder on an active particle, there will be a higher charge transfer resistance at the active particle interface [13]. Therefore, the electrode interfacial impedance decreases with increase of active particle loading, as shown in Figure 13 (a) and (b). Notice that, in the diffusive impedance region, no change in phase is observed

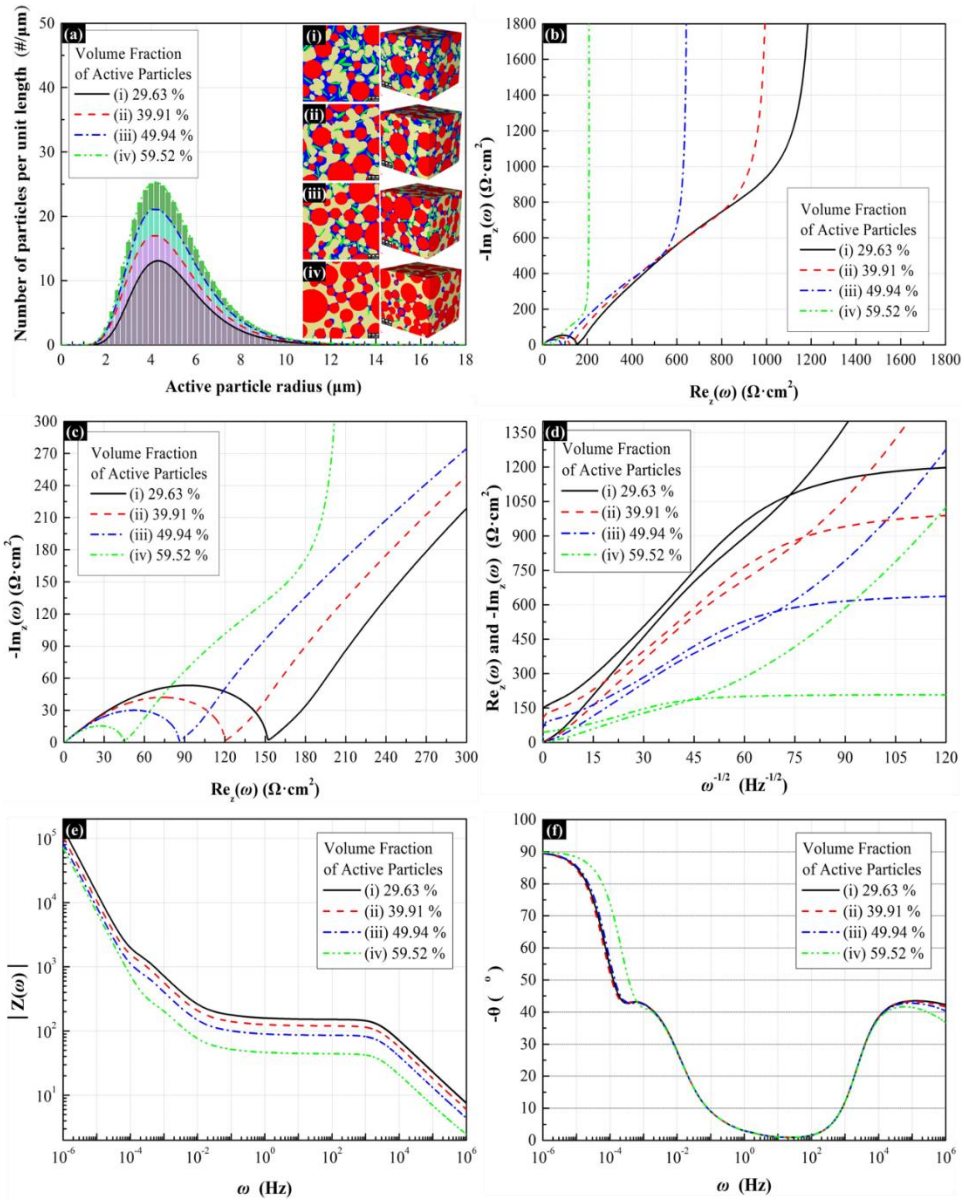

Figure 13. Dependence of the impedance response on the volume fraction of the active materials. Mean radius of spherical active particles is approximately 5 μm (i. 5.074 μm, ii. 5.0017 μm, iii. 5.0196 μm, iv. 5.0158 μm). The ratio of additive to PVDF is 0.3:1. The volume fraction of electrolyte is 35 %. The electrical conductivity of liquid-phase materials is 1.0E-2 S/cm. The specific surface areas of active particles in the electrodes are (i) 1412.3969 cm^{-1}, (ii) 1875.3419 cm^{-1}, (iii) 2343.8790 cm^{-1}, and (iv) 2796.5195 cm^{-1}. The mean effective conductivities of solid-phase materials of (i), (ii), (iii), and (iv) are 1.378E-6 S/cm, 1.661E-6 S/cm, 2.607E-6 S/cm, and 8.265E-6 S/cm, respectively. (a) Active particle size distribution function. Magnified view of Nyquist image (b) close to origin is shown in image (c). (d) Warburg plot of impedance response. (e) Magnitude image. (f) Phase angle plot.

between structures, as expected based on Figure 10. To further clarify the effect of active material surface area on impedance, a Warburg plot, Figure 13 (d), is constructed. This type of plot is usually employed to measure diffusion coefficients by examination of slope in the diffusive region, but in this case, since diffusion coefficients are fixed between electrode structures, difference in diffusive slope between structures is solely due to changing specific surface area.

Effect of Morphology of Active Materials on Diffusion Impedance Response of the 3D Electrode Microstructure

W. Lai et al and J. Song et al have previously researched the effect of morphology of active materials on diffusion impedance response by using the characteristic diffusion length of spherical, cylindrical, and platelet active particles [44, 54]. However, if an active particle shape is complex or there exists an agglomerate particle in the microstructure electrode, it is difficult to define transfer functions for diffusion impedance response due to mathematical complexity. In this paper, we consider the Sauter mean particle, as discussed in chapter 2 with a focus on estimating the diffusion impedance response of randomly structured particles. The hypothetical particle has the same mean effective surface area per unit volume as that of the given particle is described in Figure 7 (a). The Sauter mean diameter of a cylindrical particle and a platelet particle is defined for the purpose of analyzing the difference in diffusion impedance response between the characteristic diffusion length of the given particle and the Sauter mean diameter as shown in Figure 7 (b).

The impact of morphology of the active materials on diffusion impedance response by using characteristic diffusion length of active particles and an effective mean particle size, or the Sauter mean particle size, has been demonstrated in Figure 14 and Figure 15. Figure 14 shows the active electrode particles to be considered for diffusion impedance response, including spherical, cylindrical, and platelet, with a characteristic diffusion length of 2um in Figure 14 (a1) and with a Sauter mean radius 2um in Figure 14 (b1). Since the deviation of particle size distribution is the same, the difference of the impedance response at low frequencies in Nyquist plots (a2) and Bode plots (a3) is more significant for particle geometry. The difference in behavior, dependent on active particle geometry, is explained by its asymptotic approximations in Warburg and capacitive regimes [54]. For curved interfaces, the diffusion response regime adds an imaginary impedance, or capacitive deviation, higher than the original Warburg formula predicts, which is caused by the platelet diffusion morphology as given in Figure 14 (a2) and (a3). This behavior is a direct consequence of the difference in flux-normal diffusion effective area, as compared to the diffusion of platelet. This trend lends itself to a description of non-platelet geometries as a series circuit consisting of the original Warburg impedance and an extra capacitance.

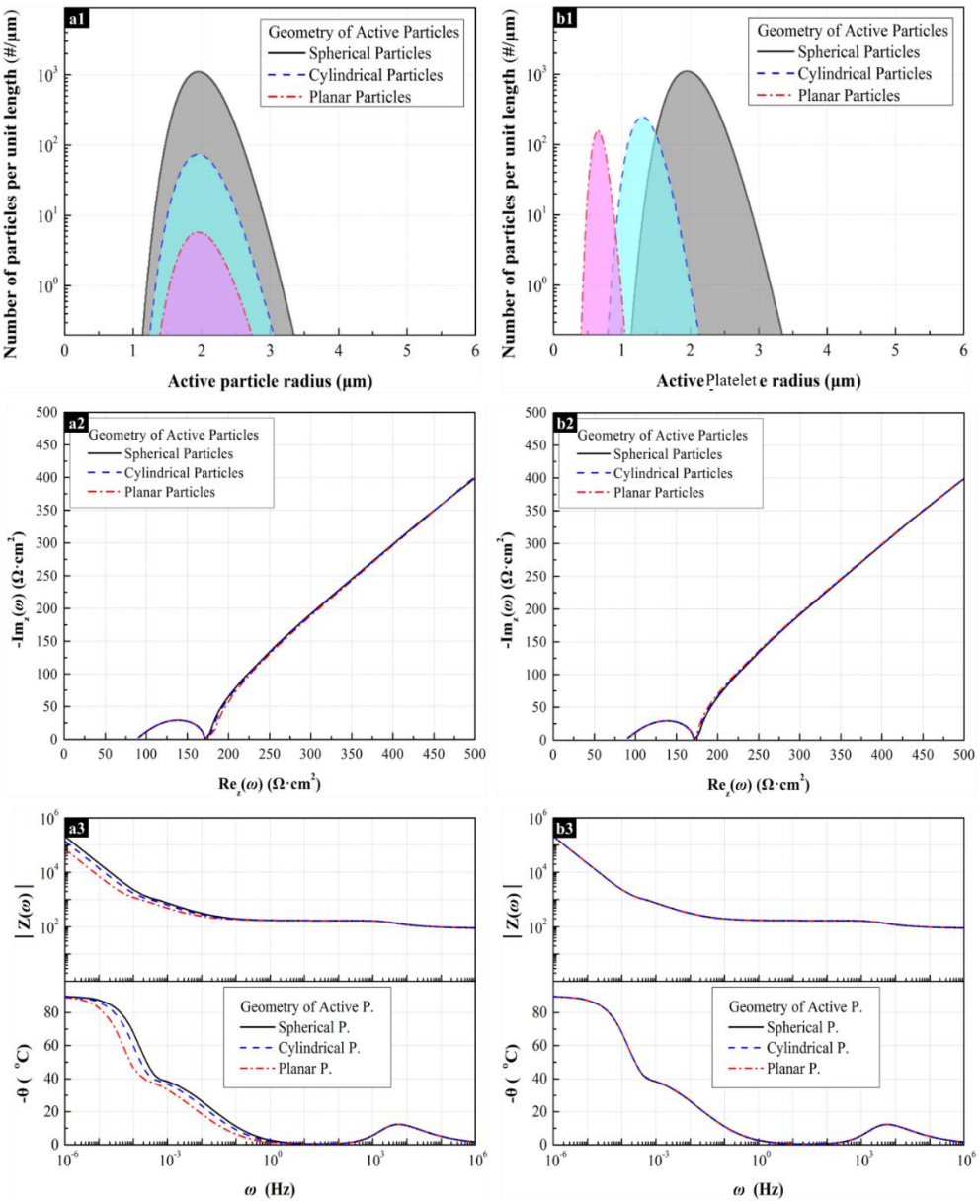

Figure 14. The morphology effect of the active material on the impedance response of the imaginary electrodes. The aspect ratios of cylindrical particles(1:γ) and platelet particles(1:α:β) are 1:10 and 1:10:10,respectively. The specific surface area of active particles is 2900 cm^{-1} and the effective conductivity of solid-phase materials is 2E-6 S/cm. The electrolyte conductivity is 5.5E-5 S/cm. (a) The characteristic mean length is 2um. The volume fractions of spherical, cylindrical, and platelet active particles are 20%, 30%, and 60%, respectively. (a1) Active particle size distribution function. (a2) Nyquist image of impedance response. (a3) Bode plots of impedance response. (b) The Sauter mean radius is 2um, and the volume fraction of active particles is 20%. (b1) Active particle size distribution function. (b2) Nyquist image of impedance response. (b3) Bode plots of impedance response.

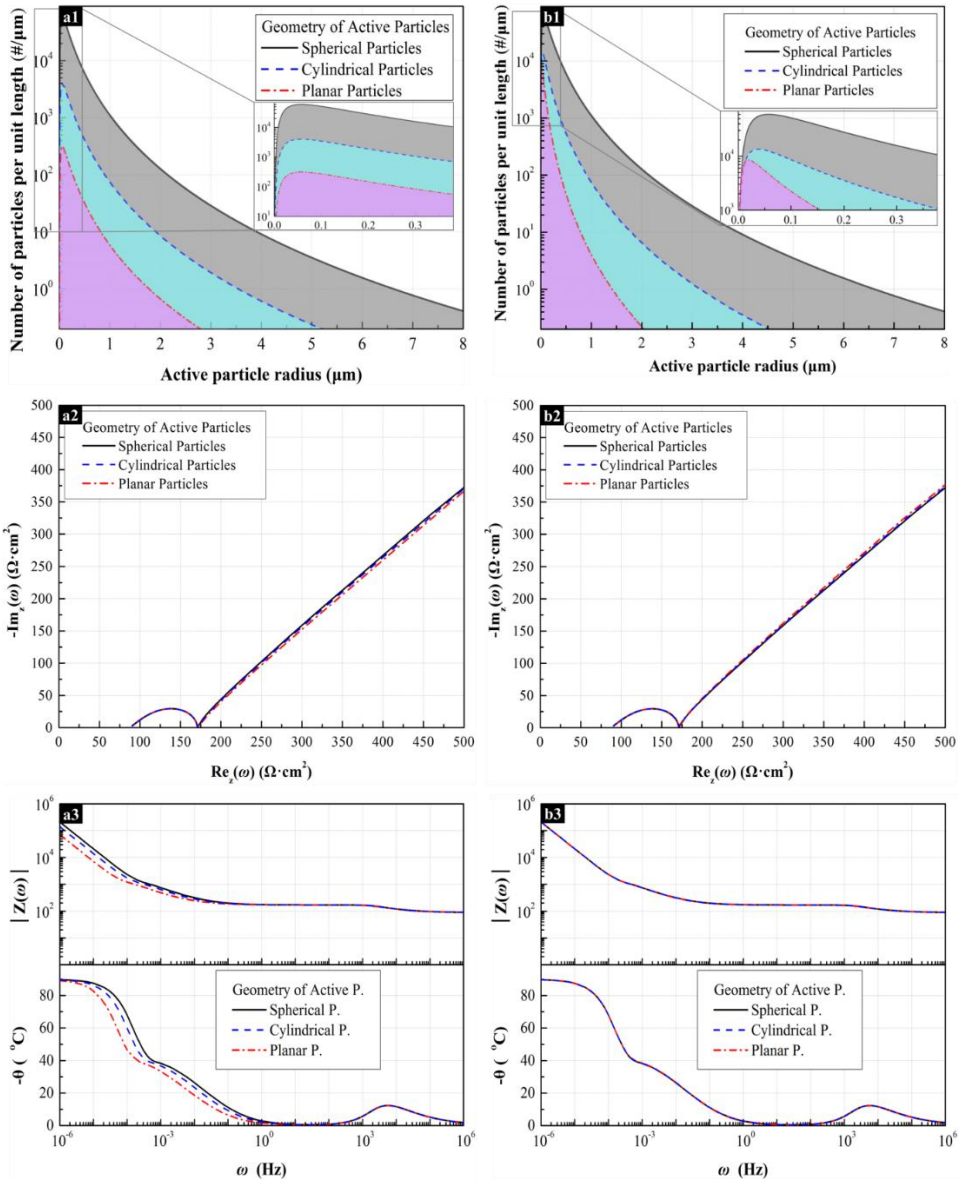

Figure 15. The morphology effect of the active material on the impedance response of the imaginary electrodes. The aspect ratios of cylindrical particles(1:γ) and platelet particles(1:α:β) are 1:10 and 1:10:10,respectively. The specific surface area of active particles is 2900 cm^{-1} and the effective conductivity of solid-phase materials is 2E-6 S/cm. The electrolyte conductivity is 5.5E-5 S/cm. (a) The characteristic mean length is 0.1333335um. The volume fractions of spherical, cylindrical, and platelet active particles are 20%, 30%, and 60%, respectively. (a1) Active particle size distribution function. (a2) Nyquist image of impedance response. (a3) Bode plots of impedance response. (b) The Sauter mean radius is 0.1333335um, and the volume fraction of active particles is 20%. (b1) Active particle size distribution function. (b2) Nyquist image of impedance response. (b3) Bode plots of impedance response.

In order to minimize the impact of morphology on the diffusion impedance response, the flux-normal diffusion effective area with regard to the distance from the active particle interface is considered by defining the Sauter mean particle size. Regardless of the original particle morphology, redefining the system in terms of Sauter mean particles with the same size distribution allows one to accurately reproduce Nyquist and Bode plots while eliminating shape effects at low frequencies, as shown in Figure 14 (b2) and (b3). This is because using the Sauter mean diameter reproduces the original particle's ratio of the external diffusion effective surface area to volume, which is related to the flux-normal diffusion effective area.

These results are not dependent on initial particle size or initial size distribution. Figure 15 displays the results of an analogous simulation, run with dramatically smaller particle size than the simulation in Figure 14 (Figure 15 (a1) and Figure 15 (b1)). Notice that, in order to keep volume fraction and specific surface area constant between the two simulations, size distribution was altered dramatically. Morphology effects similar to those in the Figure 14 are observed in Figure 15 (a2) and (a3), but show a more uniform impedance slope in the diffusive regime in accordance with the relatively increased size distribution, as previously demonstrated in Figure 10. Regardless, the morphology effect is still drastically reduced by remodeling in terms of the Sauter mean particle (Figure 15 (b2) and Figure 15 (b3)).

To understand the morphology effect and the electrical conductivity effect on the impedance response of the microstructure electrode, active particles of different shape, but all with a 3um Sauter mean radius, are considered in Figure 16. The spherical,

cylindrical, and platelet active materials are designed to have identical specific surface areas and volume fractions. The electrodes are also designed to have the same heterogeneity in active particle size. Figure 16 shows a dramatic change in semicircle diameter between shape profiles, despite all electrodes having the same specific surface area of active particles, as discussed in Figure 12. This effect may be explained by reasoning that, since platelet and cylindrical particles at the same volume fraction enable better alignment for electrical paths than spherical particles, relatively higher electrical conductivity is indicated at platelet or cylindrical geometry. This results in a smaller semicircle for the platelet and cylindrical particle electrodes. Due to being designed identical Sauter mean diameter and active particle size distribution in the porous microstructures, diffusion impedance at the Warburg impedance frequency should be drawn as similar behaviors. However, the result shows the huge differences because of different electrical conductivities, as shown in Figure 16.

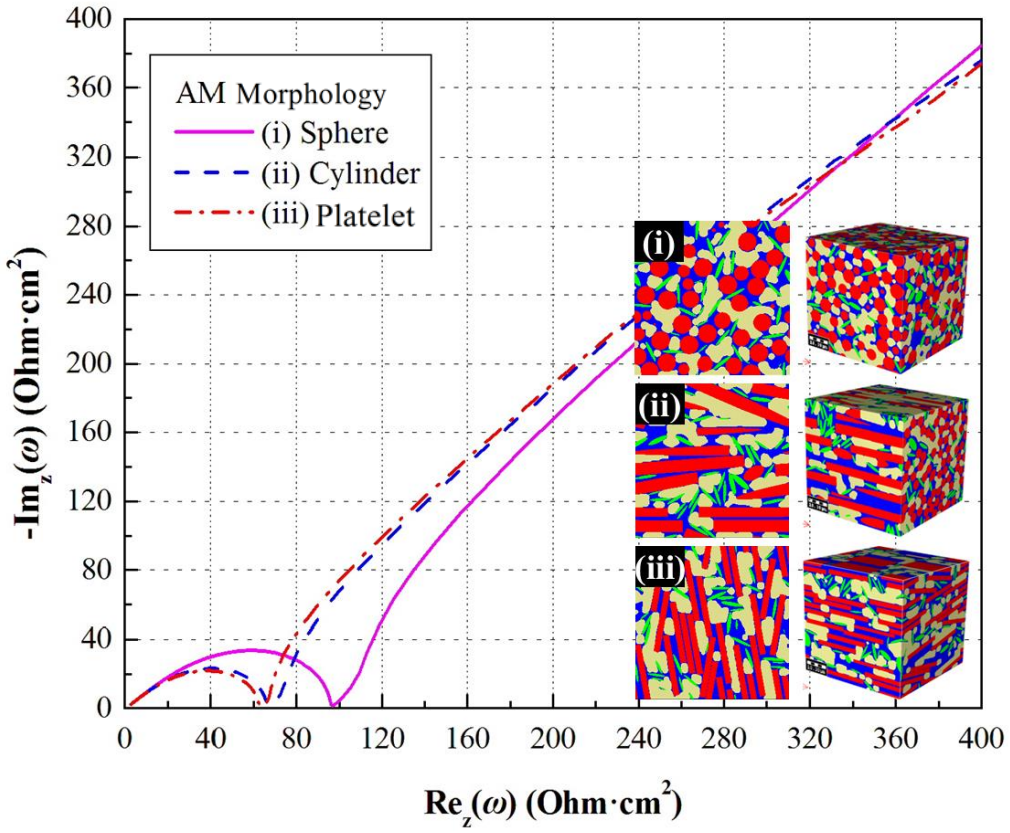

Figure 16. Morphology effect of the active material on the impedance response of the 3-D microstructure electrode. Sauter mean radius is 3um and the volume fraction of active materials is 35%. The specific surface area of active particles is approximately 1900 cm^{-1} (i. 1914.82 cm^{-1}, ii. 1920.72 cm^{-1}, iii. 1885.58 cm^{-1}). The ratio of additive to PVDF is 0.3:1. The volume fraction of electrolyte is 35 %. The effective conductivities of solid-phase materials of (i), (ii), and (iii) are 4.27E-7 S/cm, 2.025E-6 S/cm, and 2.094E-6 S/cm, respectively.

CHAPTER IV

EFFECT OF THE CHEMICAL DEGRADATION ON IMPEDANCE RESPONSE

In order to estimate the life of the battery systems, a lot of studies have been conducted. Various aging mechanisms in the systems have been identified for the last several decades. The major sources such as solid electrolyte interphase (SEI) and fracture for aging generate in the electrode [53, 86]. Solid electrolyte interphase (SEI) which is a passive film is formed at the negative electrode due to unstable electrolytes at the operating potential [87]. The result of electrolyte decomposition at the interfaces between the electrode and electrolyte forms a protecting solid layer on the surface of the active material. The main reason of the irreversible capacity loss for the first few cycles is SEI [5, 25, 64].

If SEI formation rate is sustained during battery operation, Li-ion batteries cannot be usable because of irreversible loss of Lithium. However, after SEI was formed initially, SEI growth rate reduces because electrolyte molecules could not travel through the SEI in order to go the active particle surface and electrons could not be conducted in the SEI. Therefore, battery has little additional SEI buildup during many charge-discharge cycles.

Mathematical Model for a Single Active Particle with SEI

In this chapter, a single intercalation particle with the SEI film is considered to interpret the effect of impedance response on the SEI. Figure 17 provides a Schematic diagram of particle-SEI and SEI-Electrolyte interface and an equivalent circuit diagram.

Firstly, we consider the equations to determine the impedance response of a single particle with the SEI film. We know the total single active particle impedance without insulating film from Eq. 15. The impedance response of a single active particle with the SEI film adds resistance of SEI, capacitance of SEI, and external interfacial impedance. Writing the total impedance response of a single particle with SEI film which relates the potential difference to the outward normal current density per unit surface area of an active particle, we find

$$Z_{T\_SEI,i} = \frac{1}{\dfrac{1}{\dfrac{Z_{far,i}Z_{dlb,1}}{Z_{far,i}+Z_{dlb,1}} + R_{SEI} + \dfrac{R_{ctr,2}}{1+ j\omega R_{ctr,2}C_{dbl,2}}} + j\omega C_{SEI}} \tag{23}$$

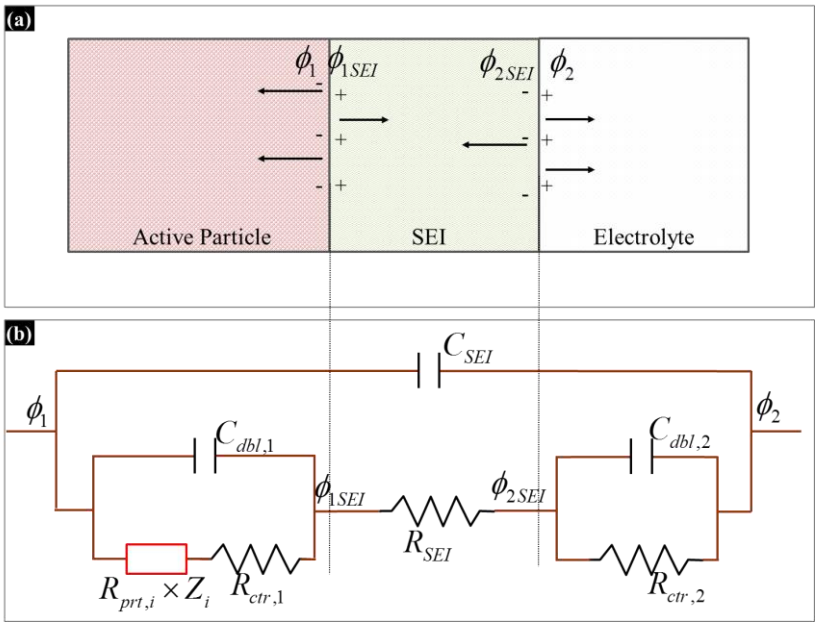

Figure 17. Schematic diagram of particle-SEI and SEI-electrolyte interface and an equivalent circuit diagram

To determine the impedance response of a single particle with the SEI film from Eq. 23, Capacity and Resistance of SEI are needed. Figure 18 provides a schematic diagram of the geometry active particles with SEI. d stands for SEI thickness. From Gauss's law which mentions that the total electric flux out of a closed surface is the same as the charge enclosed divided by the dielectric constant, the electric field can be defined as

$$E_{electric,i} = \frac{Q}{\varepsilon A_i} \tag{24}$$

where Q is the total charge enclosed within the SEI, A is the surface area, and ε is the dielectrical constant, permittivity. The voltage between particle-SEI interface and SEI-Electrolyte interface can be found by integrating the electric field:

$$\Delta V_i = \frac{Q}{\varepsilon}\int_{R_{i1}}^{R_{i2}} \frac{1}{A_i} dr \tag{25}$$

Therefore, we know the capacitance from the definition of capacitance.

$$C_i = \frac{Q}{\Delta V_i} \tag{26}$$

Capacity of the SEI on a single active particle with various morphologies shows in Table 2. In addition, the resistance of SEI between particle-SEI interface and SEI-Electrolyte interface can be defined from the definition of resistance. The resistance of SEI can be found:

$$dR_{SEI,i} = \frac{\rho}{A_i} dr \tag{27}$$

The resistance of SEI can be calculated by integrating between particle-SEI interface and SEI-Electrolyte interface, as shown in Table 3.

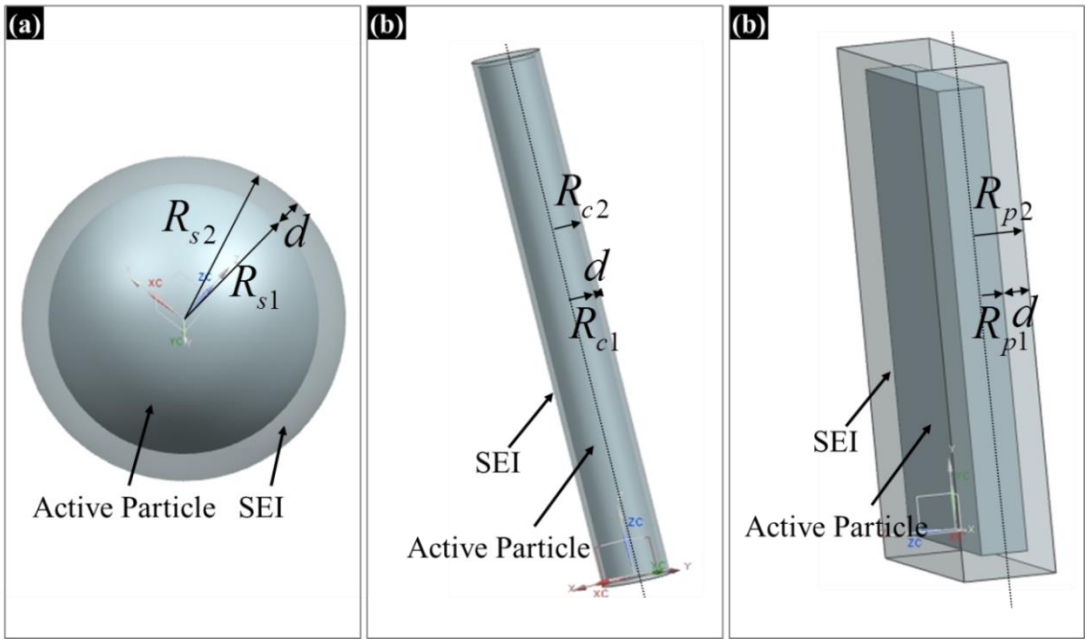

Figure 18. Schematic diagram of intercalation active particle with solid electrolyte interphase. (a) Spherical particle. (b) Cylindrical Particle. (c) Platelet Particle

Table 3. Capacity of SEI film with various morphologies.

Morphology	The SEI Capacity(F/cm^2)	The SEI Resistance (Ωcm^2)
Sphere	$\frac{\varepsilon(R_{s1}+d)}{d \cdot R_{s1}}$	$\frac{\rho_{SEI} \cdot d \cdot R_{s1}}{R_{s1}+d}$
Cylinder	$\frac{\varepsilon}{R_{c1}} \cdot \frac{1}{\ln((R_{c1}+d)/R_{c1})}$	$\rho_{SEI} \cdot R_{c1} \cdot \ln((R_{c1}+d)/R_{c1})$
platelet	$\frac{\varepsilon}{d}$	$\rho_{SEI} \cdot d$

Table 4. Electrode parameters for use in single particle simulations with SEI film**.**

Property	Value
i_0	0.69 x 10^{-3} A/cm^2
T	298 K
$\alpha_a + \alpha_c$	1
$C_{dl,1}$	1 x 10^{-5} F/cm^2
ρ_{SEI}	1.1 x 10^7 Ω cm
$C_{dl,2}$	1 x 10^{-5} F/cm^2
$R_{ct,2}$	4.4 Ω cm^2
ε	8.854187817 x 10^{-13} F/cm

As we determine SEI resistance and SEI capacity analytically, the capacity of SEI decreases and the SEI resistance increases with increasing the SEI thickness.

Impedance Response for a Single Intercalation Particle Consisting of an SEI

Simulations were performed in the condition of Table 4. To analyze the effect of SEI formation on the impedance response of the single spherical active particle, the SEI on an active particle is considered in Figure 19. The impedance response of the active particle increase when the formation of SEI layer on the active particle surface is considered. The size of the semicircles for charge transfer resistance of the active

particle and the diffusion impedance at low frequency regime does not change the shape because SEI formation does not have an influence on charge transfer resistance and diffusion impedance of the active particle. Since the SEI layer has capacitance and resistance, another semicircle on the Nyquist plot exists similar to coating effect. Chung et al. shows impedance spectra for the process of SEI formation. This spectrum also shows two different semicircles on Nyquist plot [88, 89].

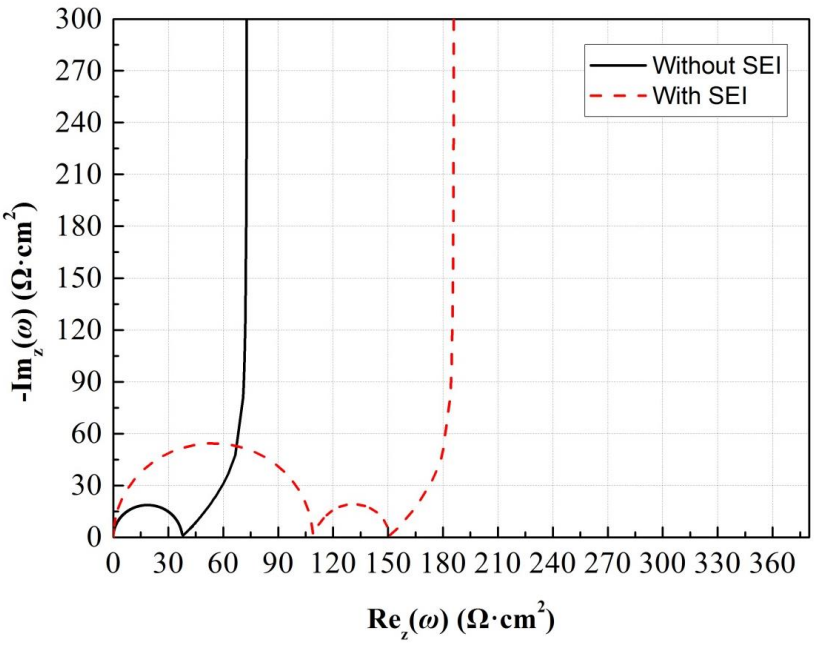

Figure 19. The effect of SEI on an active spherical particle. Active particle radius is 8 μm. SEI thickness is 0.1 μm. Capacity of SEI film is 1.0E-10 F/cm^2.

The impact of SEI thickness on total impedance response of an active spherical particle has been demonstrated in Figure 20. The SEI thickness between 1.0 and 4 μm has been considered. In order to see only thickness effect, the capacitor of the SEI is assumed as a constant input value 1.0E-11 F/cm2, which come from experimental data [53]. The image provides a larger semicircle with increasing the SEI film thickness due to the resistor of SEI. As we discussed in Figure 19, the behavior of charge transfer impedance of the active material and the diffusion impedance of the active material in Figure 20 does not depend on the SEI thickness. Since SEI thickness is two large and it have large resistance, the interfacial impedance of SEI which mentions the first large semicircle is much higher than it of the single active particle which shows the second small semicircle.

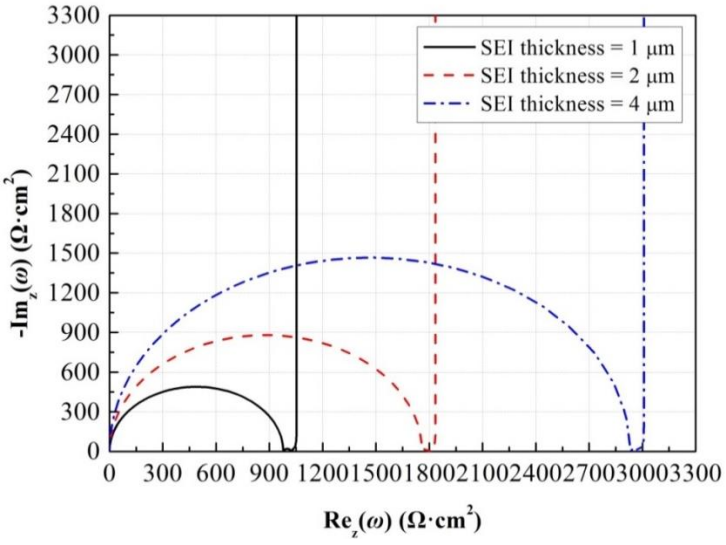

Figure 20. The effect of SEI film resistance dependent on SEI thickness of an active spherical particle. Active particle radius is 8.5 μm. Capacity of SEI film is 1.0E-11 F/cm^2.

The impedance response, dependent on the SEI formation on the active spherical particle surface, is demonstrated in Figure 21. In this Figure, variable capacities dependent on the SEI thickness are considered. The capacity of SEI $\cong \varepsilon / d$ and the SEI resistance $\cong \rho_{SEI} \cdot d$ because provided SEI thickness is much smaller than the active particle. That's why this result explains that an increase in the SEI film thickness results in an increase of the total impedance of the single spherical active particle. The Nyquist image shows that charge transfer resistance and diffusion impedance also independent on the SEI layer thickness.

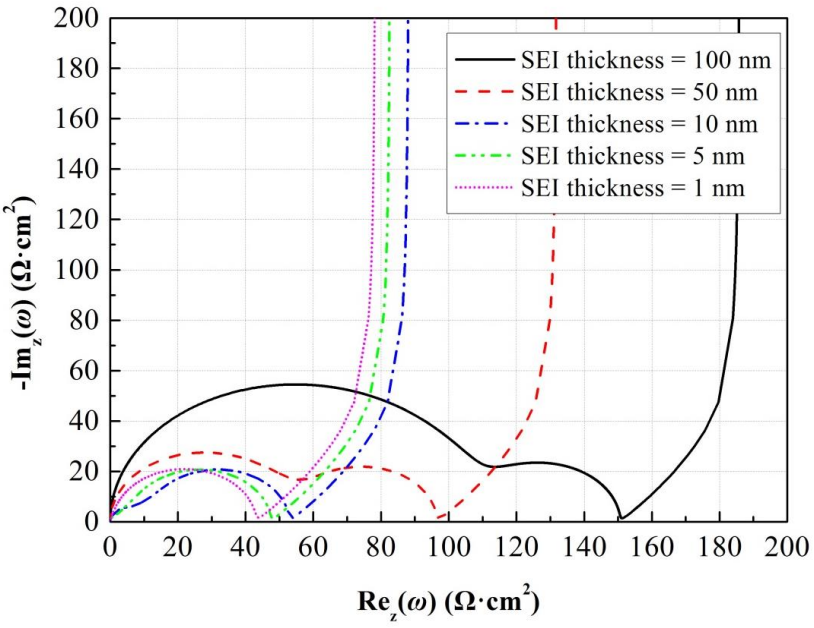

Figure 21. The effect of SEI film resistivity and Capacity dependent on SEI thickness of an active spherical particle. Active particle radius is 8.5 μm.

The simulated impedance reponse of the single active particle with SEI layer is illustrated in Figure 22 as a function of the radius of a active particle. SEI thickness is considered as 0.05 μm. As we discussed in Figure 21, the capacity and the resistance of SEI layer do not depend on the active particle radius but rely on the SEI thickness. Therefore, the first semicircle at high frequency for the SEI film and the second semicircle at mid-frequency which corresponds to charge transport at the active particle are almost identical due to the same SEI thickness. However, the diffusion impedance at low frequency increases with increasing the radius of a active particle due to a increase of the diffusion length.

The SEI layer with various geometries of an active spherical particle is now used to understand the impedance response of the SEI with various morphologies as shown in Figure 23. Because of the morphology of each particle, there exist very small differences of SEI film resistance and capacity. The first semicircles at high frequency for passivated SEI layer show the small differences. At low frequency for diffusion impedance, the differences result from various morphologies.

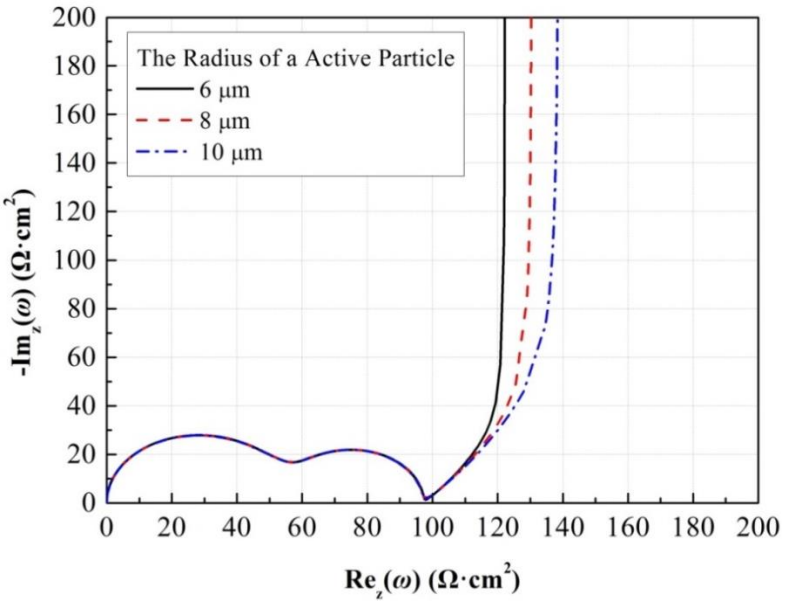

Figure 22. The impedance response of the effect of an active spherical particle radius with SEI. SEI thickness is 0.05 μm.

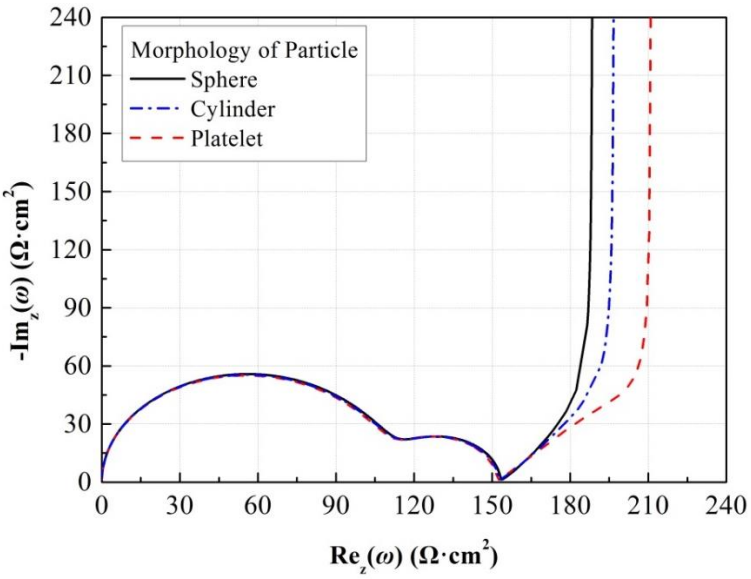

Figure 23. The effect of SEI with various morphologies of an active spherical particle. Active particle characteristic length is 8.5 μm. SEI thickness is 0.1 μm.

CHAPTER V

EFFECT OF THE MECHANICAL DEGRADATION ON IMPEDANCE RESPONSE

During operation Lithium intercalation and de-intercalation happens within the electrode active particles. During lithiation, Li ions move inside the active particles causing it to swell. On the other hand, delithiation makes the particles devoid of Li ions, which gives rise to significant amount of contraction. Periodic swelling and contraction due to lithiation and delithiation creates large amount of diffusion induced stress (DIS) within the active particles. This DIS has the potential to cause fracture within the active particles. Figure 24 shows the fracture in a graphite anode material.

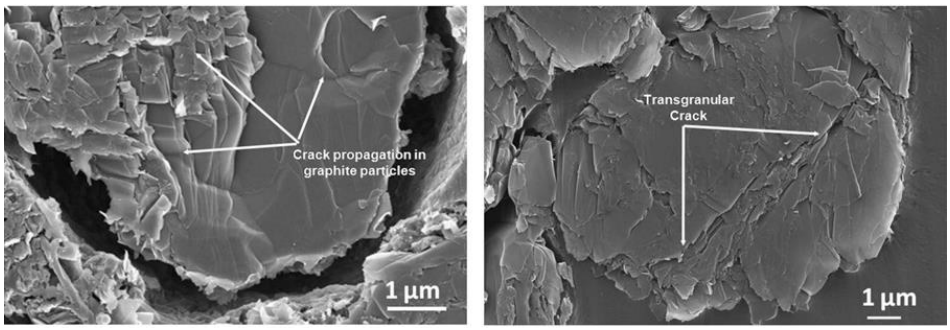

Figure 24. Brittle fracture in cylindrical graphite anode material [90]

To capture the amount of diffusion induced fracture within the active materials, a lattice spring based model has been developed [49]. In the lattice spring method, the entire domain is discretized into multiple equally spaced points, also called nodes. All

the nodes are connected by a spring as shown in Figure 25. Entire mass of the system is assumed to be equally distributed in each of the nodes. Being a quasistatic analysis, mass of the system does not affect the simulation results here. If dynamic response were to be analyzed, the distribution of mass would have been a very important aspect. Each spring in the lattice spring model which connects two nodes, displays axial as well as shear stiffness. During Li insertion or extraction, the lattice spring system deforms to ensure equilibrium at each node. Deformation of the springs induces internal force on each of them and it is stored in the form of strain energy. If the strain energy in a particular spring exceeds its fracture threshold, it breaks, and generates a micro-crack. During an entire lithiation or delithiation process, many bonds break and give rise to multiple micro-cracks. These micro-cracks can be considered as voids within the solid material.

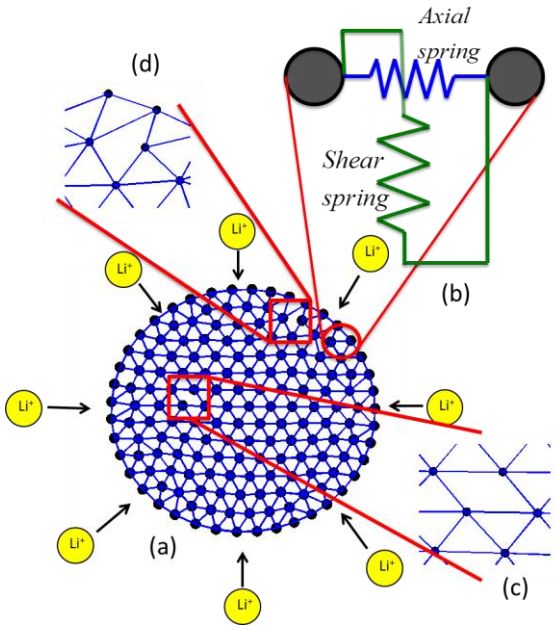

Figure 25. Random lattice spring method [49]

Lithium ions diffuse through the intact solid material without any hindrance when there is no fracture. Formation of mechanical damage introduces micro-cracks within the domain which hinders the free diffusion of Li ions. The obstacles in the form of micro-voids increase the diffusion length which results in increased tortuosity. As a result the effective diffusivity at locations where micro-cracks developed decreases significantly. Generation of multiple micro-cracks reduces the local diffusivity at multiple points within the electrode active particle. This reduction in diffusivity results in change of concentration distribution and the increment of diffusion impedance at low frequencies of the active particle as shown as shown in Figure 26.

Figure 27 shows the spherical active particle size effect of mechanical degradation with impedance response. During the discharging process at constant flux condition, a large particle leads to high concentration difference and results in generating more micro-cracks. Since fracture affects the diffusion impedance of the active particle, the diffusion impedance difference between the active particle with fracture phenomenon and the active particle without fracture increases with increasing the active particle radius. At lower frequencies, the various particle sizes results in variation of the local diffusion impedance due to various diffusion length, as shown in the Nyquist image.

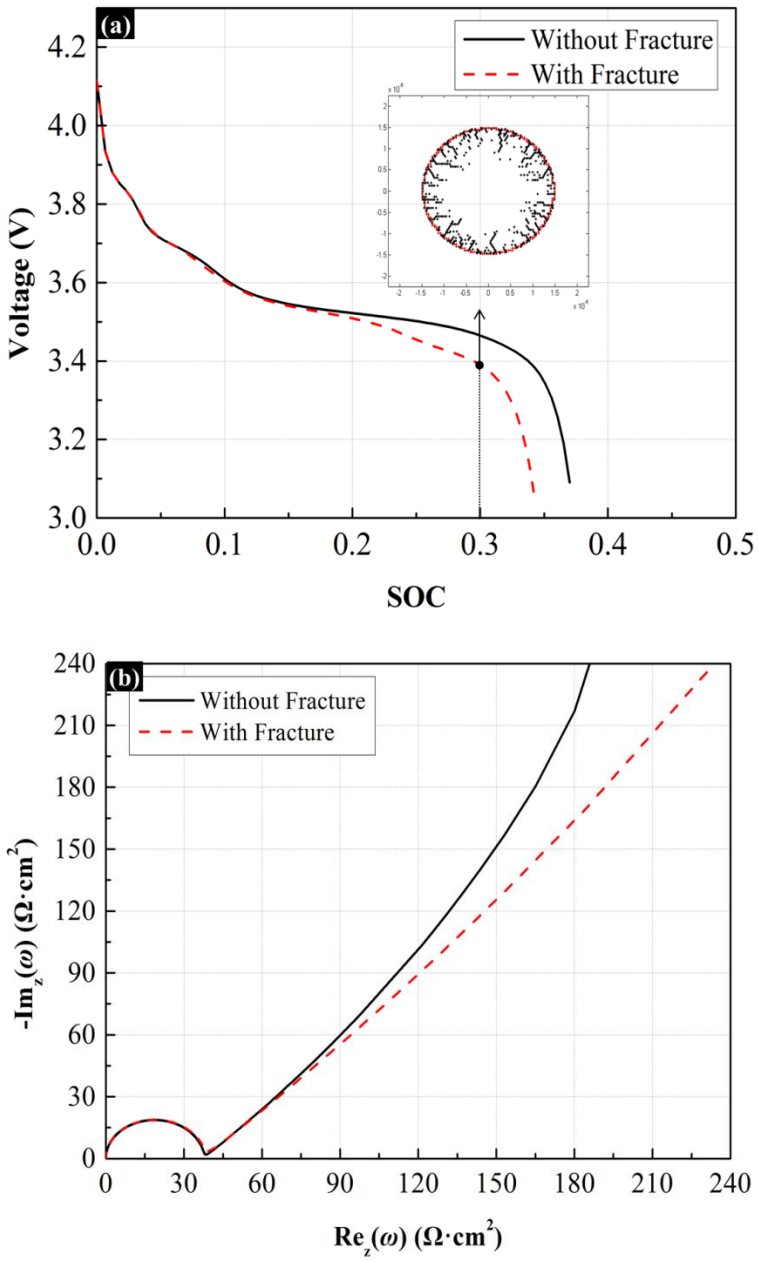

Figure 26. The effect of mechanical degradation by coupling diffusion induced fracture with impedance response of an active spherical particle. The particle radius is 15 μm. (a) Comparison between discharge profiles at 4C with diffusion induced fracture and without it. (b) Nyquist plot at x = 0.304.

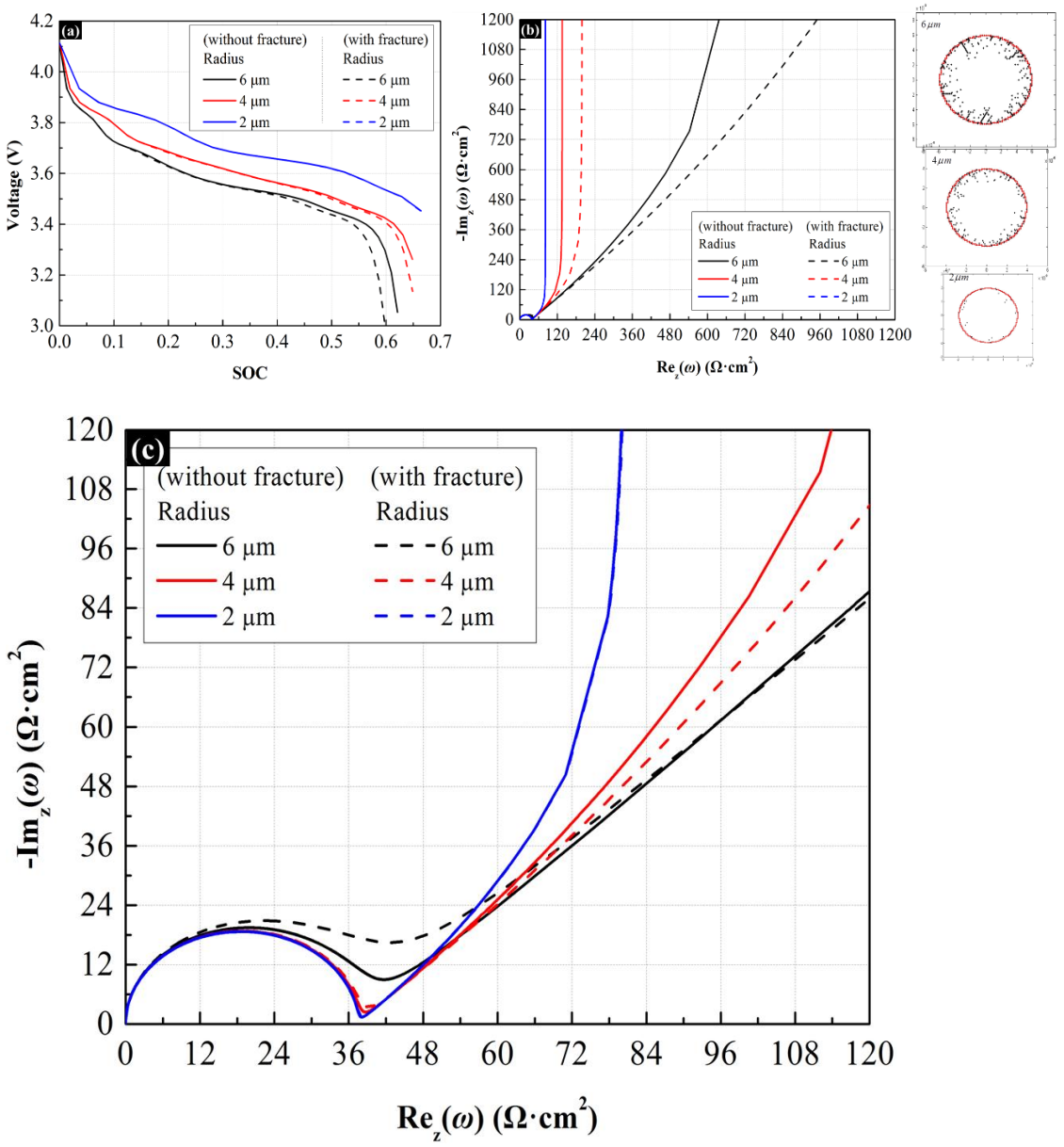

Figure 27. The spherical active particle radius effect of mechanical degradation with impedance response. (a) Comparison between discharge profiles at 4C with diffusion induced fracture and without it. Magnified view of Nyquist image (b) at x = 0.595 close to origin is shown in image (c).

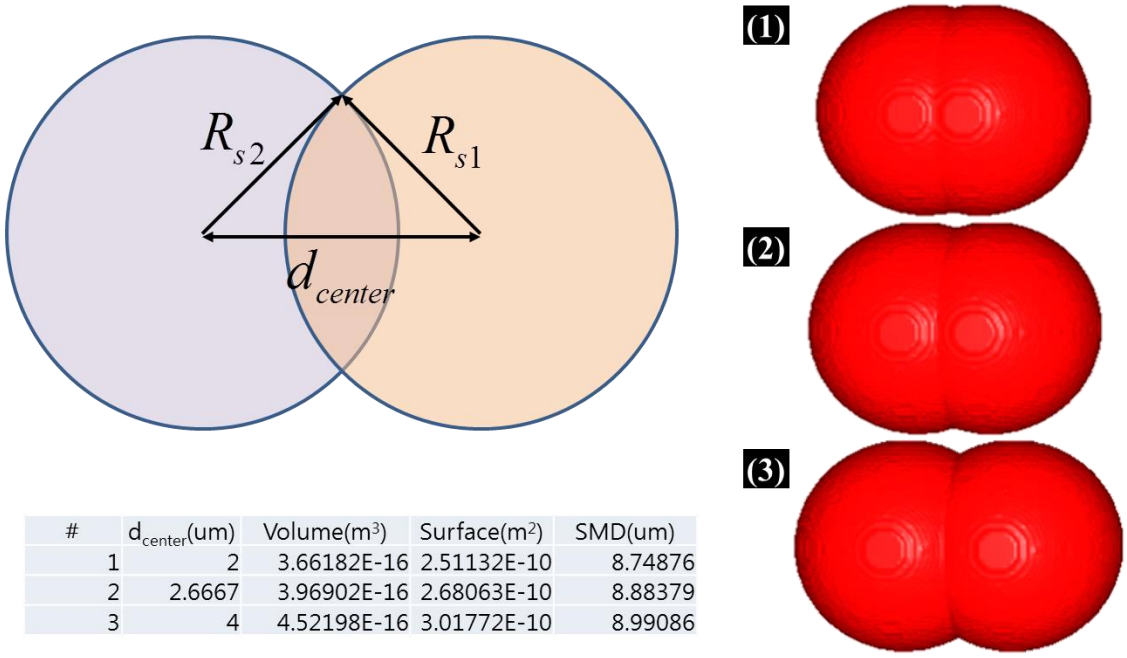

#	d_{center}(um)	Volume(m^3)	Surface(m^2)	SMD(um)
1	2	3.66182E-16	2.51132E-10	8.74876
2	2.6667	3.96902E-16	2.68063E-10	8.88379
3	4	4.52198E-16	3.01772E-10	8.99086

Figure 28. The image of agglomerate active particles with Sauter mean diameter. R_{s1} and R_{s2} are $4\mu m$.

In order to analysis the impedance response of amorphous particles in analytical method, we need to define the equivalent characteristics description for electrochemical impedance of the amorphous active particle. The Sauter mean diameter of agglomerate particles is defined for the purpose of analyzing the diffusion impedance response of an agglomerated particle. Figure 28 explains the sauter mean diameter of agglomerate active particles. The concept of the Sauter mean diameter or surface mean diameter is widely used in the field where the effective surface area is of most interest, such as in reaction and absorption research. Figure 28 shows the relationship between an agglomerate particle and a Sauter mean particle. Sauter mean diameter is the diameter of

a sphere that has the same ratio of volume to active surface area and can characterize the particles with different shapes, which was given by Eq. 14. Proposed agglomerated particles are used in Figure 29. During the discharging process, large amount of diffusion induced stress within the active particles is generated. This stress makes fracture inside of the active particle and results in the increment of diffusion impedance at low frequency regime of the active particle as shown in Figure 29 (b).

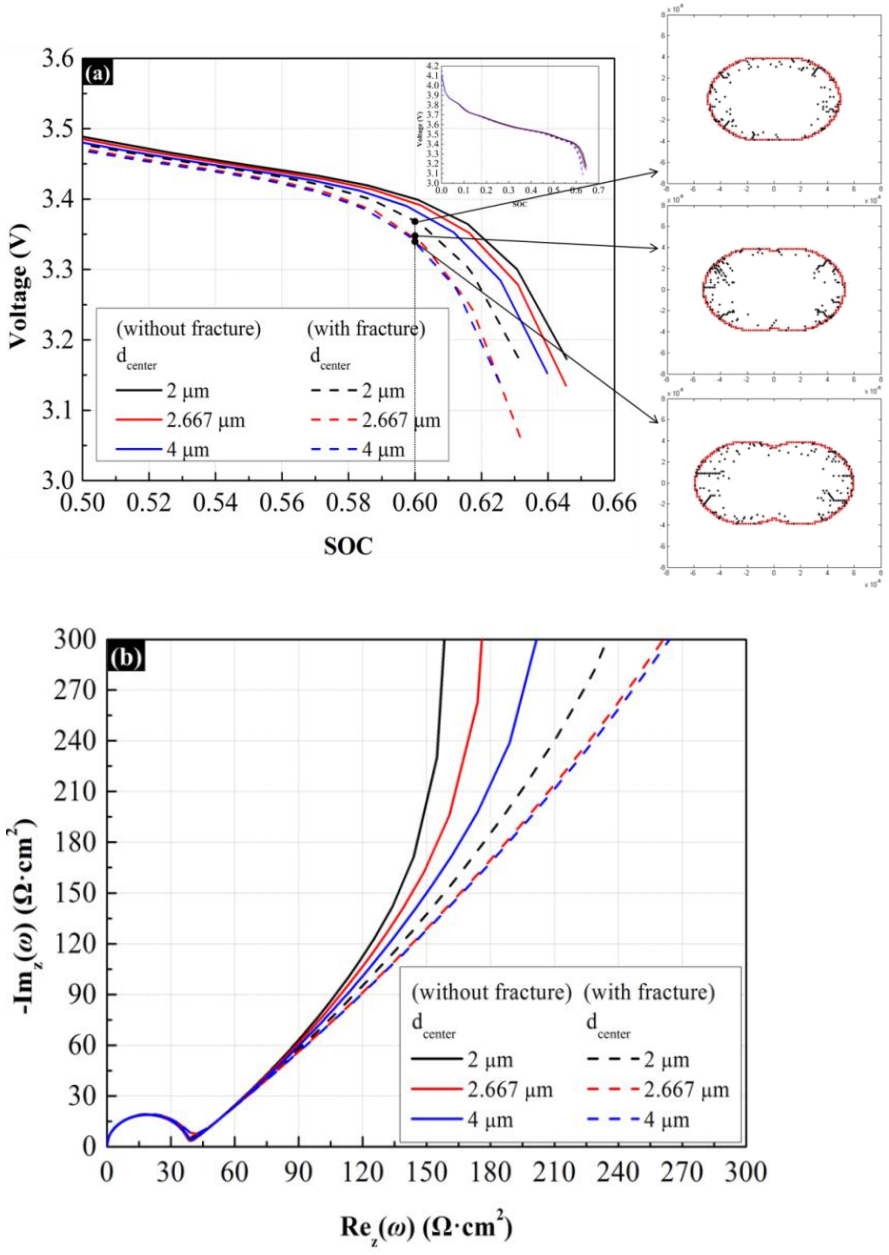

Figure 29. The agglomerate active particle effect of mechanical degradation with impedance response. (a) Comparison between discharge profiles at 4C with diffusion induced fracture and without it. Nyquist image at x = 0.6 is shown in image (b).

CHAPTER VI

SUMMARY AND OUTLOOK

In this study, the coupling of the stochastic electrode microstructures to the solid state diffusion impedance response is put forward. A model is proposed that accounts for the effect of effective electrical conductivity on the overall impedance response of 3-D electrode microstructures. It additionally captures not only the impact of the electro-active specific surface area and volume fraction of active particles on the impedance response, but also the impact of diffusion length distribution of the particles.

We have demonstrated how electrode active particle morphology has a demonstrable effect on impedance response at low frequencies due to differing flux-normal diffusive active areas, and therefore differing characteristic diffusion lengths, at equal volumes. We have also demonstrated that this shape effect may be mitigated by remodeling the particles as Sauter mean particles of the same size distribution. This method practically reproduces Electrochemical Impedance Spectroscopy results while eliminating differences due to particle morphology, allowing for modeling of even amorphous particles, for which a diffusive transfer function is difficult, if not impossible, to define in an analytical approach.

Furthermore, in order to find relevant aging mechanisms of dynamic systems, chemical degradation on the impedance response and mechanical degradation induced increase in impedance have been considered. The effect of SEI formation which results in irreversible loss of charge has been carried out to analyze the impedance response of

the single active material. The SEI formation is one of the main reasons for increase in impedance of active materials in LIB electrode. The SEI film affects interfacial impedance at high frequency since the SEI film - which is a passive solid layer - forms on the surface of an active particle. Diffusion impedance and charge transfer impedance of an active material is not affected by the SEI formation in this simulation, and the interfacial impedance of SEI layer is controlled not by an active particle size but the SEI thickness; the SEI thickness is usually much smaller than the size of an active particle.

Furthermore, the influence of the electrochemical impedance of a single active material dependent on diffusion induced stress and fracture inside the active material has been described. Fracture inside the battery electrode, which results in mechanical degradation, causes an increase in diffusion impedance at low frequency. Changes in the active material size and morphology are used to determine the impact on the electrochemical impedance response, which in turn will have an impact on fracture formation within an active particle. This allows for a correlation between active particle size and morphology and battery performance. Also, the diffusion induced fracture of an agglomerate active particle is considered by using the Sauter mean particle, which is the equivalent characteristic description of impedance response of an active material. Thus, this approach will offer a theoretical framework to elucidate the diffusion impedance behavior of a battery electrode.

Future Work

The results of this study should ultimately be used to estimate porous electrode characteristics. However, the ability to analyze the electrochemical impedance response is limited due to the analytical approach utilized and the mathematical complexity of electrochemical impedance response of a microstructure electrode. Developing more accurate predictive direct numerical approaches to explain electrochemical impedance response on electrode microstructure, SEI formation, and diffusion induced stress and fracture is needed.

In addition, we are interested in the effect of impedance response of the porous electrode on the SEI layer and fracture formation. If diffusion induced fracture is considered inside of the SEI layer, we can expect that the irreversible capacity loss can not only occur for the first few cycles but also increase continuously on LIB electrode. Fracture occurring inside of the SEI layer can be a critically negative effect for LIBs.

Finally, experimental results are required to validate any EIS solution. Once verification of system level results is complete, models can then be used to better investigate behavior at the scales considered in this study, which will lend further insight into impedance response of electrode microstructure.

REFERENCES

1. Takami, N., et al., *Electrochemical kinetics and safety of 2-volt class li-ion battery system using lithium titanium oxide anode.* Journal of the Electrochemical Society, 2009. **156**(2): p. A128-A132.

2. Newman, J. and W. Tiedemann, *Porous-electrode theory with battery applications.* Aiche Journal, 1975. **21**(1): p. 25-41.

3. Li, C.C. and Y.W. Wang, *Binder distributions in water-based and organic-based LiCoO2 electrode sheets and their effects on cell performance.* Journal of the Electrochemical Society, 2011. **158**(12): p. A1361-A1370.

4. Ebner, M., et al., *X-ray tomography of porous, transition metal oxide based lithium ion battery electrodes.* Advanded Energy Materials, 2013: p. 1-6.

5. Aurbach, D., et al., *On the correlation between surface chemistry and performance of graphite negative electrodes for li- ion batteries.* Electrochimica Acta, 1999. **45**(1-2): p. 67-86.

6. Vu, A., Y.Q. Qian, and A. Stein, *Porous electrode materials for lithium-ion batteries - how to prepare them and what makes them special.* Advanced Energy Materials, 2012. **2**(9): p. 1056-1085.

7. Biesheuvel, P.M., Y.Q. Fu, and M.Z. Bazant, *Diffuse charge and faradaic reactions in porous electrodes.* Physical Review E, 2011. **83**(6): p. 061507.

8. Shu, D., et al., *Electrochemical investigations on electrostatic spray deposited LiMn2O4 films.* Journal of Power Sources, 2003. **114**(2): p. 253-263.

9. Dokko, K., et al., *Kinetic characterization of single particles of LiCoO2 by ac-impedance and potential step methods.* Journal of the Electrochemical Society, 2001. **148**(5): p. A422-A426.

10. Costa, F.R., D.V. Franco, and L.M. Da Silva, *Electrochemical impedance spectroscopy study of the oxygen evolution reaction on a gas-evolving anode composed of lead dioxide microfibers.* Electrochimica Acta, 2013. **90**: p. 332-343.

11. Xu, S.D., et al., *Impedance spectra of nonhomogeneous, multilayered porous composite graphite electrodes for li-ion batteries: experimental and theoretical studies.* Journal of Physical Chemistry C, 2011. **115**(18): p. 9210-9219.

12. Liu, G., et al., *Effects of various conductive additive and polymeric binder contents on the performance of a lithium-ion composite cathode.* Journal of the Electrochemical Society, 2008. **155**(12): p. A887-A892.

13. Liu, G., et al., *Particles and polymer binder interaction: a controlling factor in lithium-ion electrode performance.* Journal of the Electrochemical Society, 2012. **159**(3): p. A214-A221.

14. Atebamba, J.M., et al., *On the interpretation of measured impedance spectra of insertion cathodes for lithium-ion batteries.* Journal of the Electrochemical Society, 2010. **157**(11): p. A1218-A1228.

15. Albertus, P., J. Christensen, and J. Newman, *Experiments on and modeling of positive electrodes with multiple active materials for lithium-ion batteries.* Journal of the Electrochemical Society, 2009. **156**(7): p. A606-A618.

16. Sato, H., et al., *Electrochemical characterization of thin-film LiCoO2 electrodes in propylene carbonate solutions.* Journal of Power Sources, 1997. **68**(2): p. 540-544.

17. La Mantia, F., J. Vetter, and P. Novak, *Impedance spectroscopy on porous materials: a general model and application to graphite electrodes of lithium-ion batteries.* Electrochimica Acta, 2008. **53**(12): p. 4109-4121.

18. Mellgren, N., et al., *Impedance as a tool for investigating aging in lithium-ion porous electrodes.* Journal of the Electrochemical Society, 2008. **155**(4): p. A304-A319.

19. Brown, S., et al., *Impedance as a tool for investigating aging in lithium-ion porous electrodes - ii. positive electrode examination.* Journal of the Electrochemical Society, 2008. **155**(4): p. A320-A338.

20. Srinivasan, V. and J. Newman, *Design and optimization of a natural graphite/iron phosphate lithium-ion cell.* Journal of the Electrochemical Society, 2004. **151**(10): p. A1530-A1538.

21. Srinivasan, V. and J. Newman, *Discharge model for the lithium iron-phosphate electrode.* Journal of the Electrochemical Society, 2004. **151**(10): p. A1517-A1529.

22. Levi, M.D. and D. Aurbach, *Impedance spectra of porous, composite intercalation electrodes: the origin of the low-frequency semicircles.* Journal of Power Sources, 2005. **146**(1-2): p. 727-731.

23. Hao, F. and D.N. Fang, *Diffusion-induced stresses of spherical core-shell electrodes in lithium-ion batteries: the effects of the shell and surface/interface stress.* Journal of the Electrochemical Society, 2013. **160**(4): p. A595-A600.

24. Kalnaus, S., K. Rhodes, and C. Daniel, *A study of lithium ion intercalation induced fracture of silicon particles used as anode material in li-ion battery*. Journal of Power Sources, 2011. **196**(19): p. 8116-8124.

25. Aurbach, D., *Review of selected electrode-solution interactions which determine the performance of li and li ion batteries.* Journal of Power Sources, 2000. **89**(2): p. 206-218.

26. Verma, P., P. Maire, and P. Novak, *A review of the features and analyses of the solid electrolyte interphase in li-ion batteries.* Electrochimica Acta, 2010. **55**(22): p. 6332-6341.

27. Arora, P., R.E. White, and M. Doyle, *Capacity fade mechanisms and side reactions in lithium-ion batteries.* Journal of the Electrochemical Society, 1998. **145**(10): p. 3647-3667.

28. Xu, K., *Nonaqueous liquid electrolytes for lithium-based rechargeable batteries.* Chemical Reviews, 2004. **104**(10): p. 4303-4417.

29. Aurbach, D., et al., *The correlation between the surface-chemistry and the performance of li-carbon intercalation anodes for rechargeable rocking-chair type batteries.* Journal of the Electrochemical Society, 1994. **141**(3): p. 603-611.

30. Kim, J.S. and Y.T. Park, *Characteristics of surface films formed at a mesocarbon microbead electrode in a li-ion battery.* Journal of Power Sources, 2000. **91**(2): p. 172-176.

31. Zhang, S.S., et al., *Understanding solid electrolyte interface film formation on graphite electrodes.* Electrochemical and Solid State Letters, 2001. **4**(12): p. A206-A208.

32. Chon, M.J., et al., *Real-time measurement of stress and damage evolution during initial lithiation of crystalline silicon.* Physical Review Letters, 2011. **107**(4): p. 045503

33. Christensen, J., *Modeling diffusion-induced stress in li-ion cells with porous electrodes.* Journal of the Electrochemical Society, 2010. **157**(3): p. A366-A380.

34. Wang, H.F., et al., *TEM study of electrochemical cycling-induced damage and disorder in LiCoO2 cathodes for rechargeable lithium batteries.* Journal of the Electrochemical Society, 1999. **146**(2): p. 473-480.

35. Gao, Y.F. and M. Zhou, *Coupled mechano-diffusional driving forces for fracture in electrode materials.* Journal of Power Sources, 2013. **230**: p. 176-193.

36. Meyers, J.P., et al., *The impedance response of a porous electrode composed of intercalation particles.* Journal of the Electrochemical Society, 2000. **147**(8): p. 2930-2940.

37. Deng, Z.F., et al., *Electrochemical impedance spectroscopy study of a lithium/sulfur battery: modeling and analysis of capacity fading.* Journal of the Electrochemical Society, 2013. **160**(4): p. A553-A558.

38. Yoon, S., et al., *Power capability analysis in lithium ion batteries using electrochemical impedance spectroscopy.* Journal of Electroanalytical Chemistry, 2011. **655**(1): p. 32-38.

39. Xu, J., et al., *A new method to estimate the state of charge of lithium-ion batteries based on the battery impedance model.* Journal of Power Sources, 2013. **233**: p. 277-284.

40. Hang, T., et al., *Electrochemical impedance spectroscopy analysis for lithium-ion battery using Li4Ti5O12 anode.* Journal of Power Sources, 2013. **222**: p. 442-447.

41. Troltzsch, U., O. Kanoun, and H.R. Trankler, *Characterizing aging effects of lithium ion batteries by impedance spectroscopy.* Electrochimica Acta, 2006. **51**(8-9): p. 1664-1672.

42. Ko, Y., I.B. Singh, and S.M. Park, *A novel method for corrosion reaction analysis by fourier transform electrochemical impedance spectroscopy: corrosion of 9Cr-1 Mo ferritic steel in 0.050M H2SO4.* Electroanalysis, 2013. **25**(4): p. 1035-1043.

43. Cruz-Manzo, S. and R. Chen, *Electrochemical impedance study on estimating the mass transport resistance in the polymer electrolyte fuel cell cathode catalyst layer.* Journal of Electroanalytical Chemistry, 2013. **702**: p. 45-48.

44. Lai, W. and F. Ciucci, *Small-signal apparent diffusion impedance of intercalation battery electrodes.* Journal of the Electrochemical Society, 2011. **158**(2): p. A115-A121.

45. Colclasure, A.M., K.A. Smith, and R.J. Kee, *Modeling detailed chemistry and transport for solid-electrolyte-interface sei-films in li-ion batteries.* Electrochimica Acta, 2011. **58**: p. 33-43.

46. He, Y.B., et al., *Effect of solid electrolyte interface sei-film on cyclic performance of Li4Ti5O12 anodes for li ion batteries.* Journal of Power Sources, 2013. **239**: p. 269-276.

47. Hao, F., X. Gao, and D.N. Fang, *Diffusion-induced stresses of electrode nanomaterials in lithium-ion battery: the effects of surface stress.* Journal of Applied Physics, 2012. **112**(10): p. 103507

48. Zhang, J.Q., et al., *Diffusion induced stress in layered li-ion battery electrode plates.* Journal of Power Sources, 2012. **209**: p. 220-227.

49. Barai, P. and P.P. Mukherjee, *Stochastic analysis of diffusion induced damage in lithium-ion battery electrodes.* Journal of the Electrochemical Society, 2013. **160**(6): p. A955-A967.

50. Hao, F. and D.N. Fang, *Reducing diffusion-induced stresses of electrode-collector bilayer in lithium-ion battery by pre-strain.* Journal of Power Sources, 2013. **242**: p. 415-420.

51. Doyle, M., J.P. Meyers, and J. Newman, *Computer simulations of the impedance response of lithium rechargeable batteries.* Journal of the Electrochemical Society, 2000. **147**(1): p. 99-110.

52. Levi, M.D. and D. Aurbach, *Impedance of a single intercalation particle and of non-homogeneous, multilayered porous composite electrodes for li-ion batteries.* Journal of Physical Chemistry B, 2004. **108**(31): p. 11693-11703.

53. Huang, R.W.J.M., F. Chung, and E.M. Kelder, *Impedance simulation of a li-ion battery with porous electrodes and spherical li+ intercalation particles.* Journal of the Electrochemical Society, 2006. **153**(8): p. A1459-A1465.

54. Song, J.H. and M.Z. Bazant, *Effects of nanoparticle geometry and size distribution on diffusion impedance of battery electrodes.* Journal of the Electrochemical Society, 2013. **160**(1): p. A15-A24.

55. Sikha, G. and R.E. White, *Analytical expression for the impedance response for a lithium-ion cell.* Journal of the Electrochemical Society, 2008. **155**(12): p. A893-A902.

56. Xu, S.D., et al., *Electrochemical impedance spectra of intercalation compound electrodes: models and theoretical simulations.* Acta Physico-Chimica Sinica, 2011. **27**(10): p. 2353-2359.

57. Sunde, S., et al., *An impedance model for a porous intercalation electrode with mixed conductivity.* Journal of the Electrochemical Society, 2009. **156**(8): p. B927-B937.

58. Svensson, A.M., L.O. Valoen, and R. Tunold, *Modeling of the impedance response of porous metal hydride electrodes.* Electrochimica Acta, 2005. **50**(13): p. 2647-2653.

59. Boukamp, B.A., *Electrochemical impedance spectroscopy in solid state ionics: recent advances.* Solid State Ionics, 2004. **169**(1-4): p. 65-73.

60. Zhu, Y.R., et al., *Kinetic study on LiFePO4-positive electrode material of lithium-ion battery.* Ionics, 2011. **17**(5): p. 437-441.

61. Schmidt, J.P., et al., *Studies on LiFePO4 as cathode material using impedance spectroscopy.* Journal of Power Sources, 2011. **196**(12): p. 5342-5348.

62. Jacobsen, T. and K. West, *Diffusion impedance in planar, cylindrical and spherical-symmetry.* Electrochimica Acta, 1995. **40**(2): p. 255-262.

63. Levi, M.D. and D. Aurbach, *Frumkin intercalation isotherm - a tool for the description of lithium insertion into host materials: a review.* Electrochimica Acta, 1999. **45**(1-2): p. 167-185.

64. Ploehn, H.J., P. Ramadass, and R.E. White, *Solvent diffusion model for aging of lithium-ion battery cells.* Journal of the Electrochemical Society, 2004. **151**(3): p. A456-A462.

65. Peled, E., D. Golodnitsky, and G. Ardel, *Advanced model for solid electrolyte interphase electrodes in liquid and polymer electrolytes.* Journal of the Electrochemical Society, 1997. **144**(8): p. L208-L210.

66. Ramadass, P., et al., *Development of first principles capacity fade model for li-ion cells.* Journal of the Electrochemical Society, 2004. **151**(2): p. A196-A203.

67. Vetter, J., et al., *Ageing mechanisms in lithium-ion batteries.* Journal of Power Sources, 2005. **147**(1-2): p. 269-281.

68. Markevich, E., M.D. Levi, and D. Aurbach, *New insight into studies of the cycling performance of li-graphite electrodes.* Journal of the Electrochemical Society, 2005. **152**(4): p. A778-A786.

69. Schranzhofer, H., et al., *Electrochemical impedance spectroscopy study of the sei-formation on graphite and metal electrodes.* Journal of Power Sources, 2006. **153**(2): p. 391-395.

70. Purkayastha, R. and R.M. McMeeking, *A linearized model for lithium ion batteries and maps for their performance and failure.* Journal of Applied Mechanics-Transactions of the Asme, 2012. **79**(3): p. 031021

71. Deshpande, R., et al., *Battery cycle life prediction with coupled chemical degradation and fatigue mechanics.* Journal of the Electrochemical Society, 2012. **159**(10): p. A1730-A1738.

72. Harris, S.J., et al., *Mesopores inside electrode particles can change the li-ion transport mechanism and diffusion-induced stress.* Journal of Materials Research, 2010. **25**(8): p. 1433-1440.

73. Christensen, J. and J. Newman, *Stress generation and fracture in lithium insertion materials.* Journal of Solid State Electrochemistry, 2006. **10**(5): p. 293-319.

74. Christensen, J. and J. Newman, *A mathematical model of stress generation and fracture in lithium manganese oxide.* Journal of the Electrochemical Society, 2006. **153**(6): p. A1019-A1030.

75. Benedek, R. and M.M. Thackeray, *Lithium reactions with intermetallic-compound electrodes.* Journal of Power Sources, 2002. **110**(2): p. 406-411.

76. Wu, H. and Y. Cui, *Designing nanostructured si-anodes for high energy lithium ion batteries.* Nano Today, 2012. **7**(5): p. 414-429.

77. Beaulieu, L.Y., et al., *Colossal reversible volume changes in lithium alloys.* Electrochemical and Solid State Letters, 2001. **4**(9): p. A137-A140.

78. Cheng, Y.T. and M.W. Verbrugge, *Application of hasselman's crack propagation model to insertion electrodes.* Electrochemical and Solid State Letters, 2010. **13**(9): p. A128-A131.

79. Woodford, W.H., Y.M. Chiang, and W.C. Carter, *Electrochemical shock of intercalation electrodes: a fracture mechanics analysis.* Journal of the Electrochemical Society, 2010. **157**(10): p. A1052-A1059.

80. Fan, L.-S. and C. Zhu, *Principles of gas-solid flows*. Cambridge Series in Chemical Engineering, 2005, Cambridge University Press. xvii: p. 557

81. Thiedmann, R., et al., *Stochastic simulation model for the 3D morphology of composite materials in li-ion batteries.* Computational Materials Science, 2011. **50**(12): p. 3365-3376.

82. Chen, Y.H., et al., *Selection of conductive additives in li-ion battery cathodes - a numerical study.* Journal of the Electrochemical Society, 2007. **154**(10): p. A978-A986.

83. Chen, X., et al., *A patterned 3D silicon anode fabricated by electrodeposition on a virus-structured current collector.* Advanced Functional Materials, 2011. **21**(2): p. 380-387.

84. Zamel, N., et al., *Estimating effective thermal conductivity in carbon paper diffusion media.* Chemical Engineering Science, 2010. **65**(13): p. 3994-4006.

85. Diard, J.P., B. Le Gorrec, and C. Montella, *Influence of particle size distribution on insertion processes in composite electrodes.* Journal of Electroanalytical Chemistry, 2001. **499**(1): p. 67-77.

86. Abraham, D.P., et al., *Diagnosis of power fade mechanisms in high-power lithium-ion cells.* Journal of Power Sources, 2003. **119**: p. 511-516.

87. Pinson, M.B. and M.Z. Bazant, *Theory of sei-formation in rechargeable batteries: capacity fade, accelerated aging and lifetime prediction.* Journal of the Electrochemical Society, 2013. **160**(2): p. A243-A250.

88. Chung, K., et al., *Impedance studies of the solid electrolyte interface of carbon anodes in lithium ion batteries.* Journal of Industrial and Engineering Chemistry, 2004. **10**(2): p. 290-294.

89. Tang, M., S.D. Lu, and J. Newman, *Experimental and theoretical investigation of solid-electrolyte-interphase formation mechanisms on glassy carbon.* Journal of the Electrochemical Society, 2012. **159**(11): p. A1775-A1785.

90. Harris, S.J., et al., *Mesopores inside electrode particles can change the li-ion transport mechanism and diffusion-induced stress.* Journal of Materials Research, 2010. **25**(08): p. 1433-1440.